International Benchmark on Numerical Simulations for 1D, Nonlinear Site Response (PRENOLIN): Verification Phase Based on Canonical Cases

International benchmark on numerical simulations for 1D, non-linear site response (PRENOLIN): verification phase based on canonical cases

Julie Régnier CEREMA, Nice, France

Luis-Fabian Bonilla IFSTTAR, Paris, France

Pierre-Yves Bard IFSTTAR/ISterre, Paris-Grenoble, France

Etienne Bertrand, CEREMA, Nice, France

Fabrice Hollender, CEA, Cadarache, France

Hiroshi Kawase, DPRI, Kyoto, Japan

Marianne Marrot, CEREMA, Nice, France

Deborah Sicilia, EDF, Aix-en-provence, France

Dominic Assimaki, Caltech, Pasadena, US

Daniela Boldini, UNIBO, Bologna, Italy

Angelo Amorosi, Politecnico of Bari, Italy

Annamaria Di Lernia, Politecnico of Bari, Italy

Gaetano Falcone, Politecnico of Bari, Italy

Anna Chiaradonna, Univ. Napoli, Napoli, Italy

Florent DeMartin, BRGM, Orléan, France

Evelyne Foerster, CEA, Saclay, France

Sebastiano Foti, Politecnico di Torino, Torino, Italy

Céline Gélis, IRSN, Fontenay-aux-roses, France

George Gazetas, NTUA, Athena, Greece

Jim Gingery, UCSD, San Diego, US

Nathali Glinsky, CEREMA, Nice, France

Joseph Harmon, Univ. Illinois at Urbana-Champaign, US

Youssef Hashash, Univ. Illinois at Urbana-Champaign, US

Susumu Iai, DPRI, Kyoto, Japan

Boris Jeremic, UCD, Davis, US

Steve Kramer, Univ. of Washington, US

Stavroula Kontoe, Imperial College, London, England

Jozef Kristek, , CUB, Bratislava, Slovakia

Giuseppe Lanzo, Univ. Rome, Rome, Italy

Fernando Lopez-Caballero, Centrale Supélec Paris, France

Diego Mercerat, CEREMA, Nice, France

Peter Moczo, CUB, Bratislava, Slovakia

Silvana Montoya, CentraleSupélec, France

Michael Musgrove, Univ. Illinois, US

Alex Nieto-Ferro, EDF, Clamart, France,

Alessandro Pagliaroli, CNR-IGAG, Rome, Italy

Federico Pisanò, TUDelft, Netherlands

Aneta Richterova, CUB, Bratislava, Slovakia

Suwal Sajana, Univ. Rome, Rome, Italy

Maria-Paola Santisi d'Avila, UNS, Nice, France

Jian Shi, Caltech, Pasadena, US

Francesco Silvestri, Univ. Napoli, Napoli, Italy

Giuseppe Tropeano, Univ. Cagliari, Cagliari, Italy.

Kohei Watanabe, Shimizu Corporation, Tokyo, Japan

0 Abstract

PRENOLIN is an international benchmark presently underway to test multiple numerical simulation codes capable of predicting non-linear seismic site response with various constitutive models. One of the objectives of this project is the assessment of the uncertainties associated with non-linear simulation of 1D site effects. A first verification phase (i.e. comparison between numerical codes on simple, idealistic cases) will be followed by a validation phase, comparing the predictions of such numerical estimations with actual strong motion recordings obtained at well-known sites. The benchmark presently involves 19 different prediction teams and 23 different non-linear computational models.

We present here the main results of the verification phase dealing with simple cases. Three different idealized soil profiles were tested over a wide range of shear strains with different input motions and different boundary conditions at the sediment/bedrock interface. A first iteration focusing on the elastic and visco-elastic cases proved to be useful to ensure a common understanding and to identify numerical issues before pursuing the non-linear modeling. Besides minor (but always possible…) mistakes in the implementation of input parameters and output units, the initial discrepancies between the numerical results can be attributed to (1) different understanding of the expression "input motion" in different communities, and (2) different implementations of material damping and possible numerical dispersion. The second round of computations thus allowed a convergence of all teams to the Haskell-Thomson analytical solution in elastic and visco-elastic cases. For non-linear computations we investigate the epistemic uncertainties related only to wave propagation modeling using different non-linear rheological models. Such epistemic uncertainties are shown to increase with the strain level and to reach values around 0.2 (natural log scale) for a 0.5 g reference motion, which may be reduced by almost 50% when the various constitutive models do use the same shear strength and damping.

1 Introduction

Including site effects in seismic hazard assessments requires the consideration, at some stage, of non-linear behavior of soils, which may greatly affect their dynamic responses to strong motion and significantly modify their amplifications behavior compared to weak motion (computed or measured). Even in areas of moderate seismicity, the hazard level at long to very long return periods (i.e., several thousands to tens of thousands years) may be large enough to generate significant strains in shallow, soft soil layers, which in turn leads to a degradation of their mechanical properties such as hysteretic behavior with loss of shear stiffness and increased energy dissipation [1–7].

Such dependence of the dynamic soil response on the level of seismic loading, conventionally denoted as "non-linear effects" [8], involves rather complex mechanical processes, which may be grouped roughly in two main origins. The first is the degradation of the mechanical properties of the material, which is often characterized by a decrease in the shear modulus coupled with an increase in energy dissipation; while the second is related to pore pressure changes in water-saturated granular soils, linked with volumetric changes of the soil skeleton under shear stress, and may generate liquefaction in loose sandy soils. Given the limited possibility of treating liquefiable soils, our interest here focused on the first type of non-linearity, without any consideration of pore water pressure generation or liquefaction.

The first type of non-linear effect (i.e. without liquefaction) was identified by geotechnical earthquake engineering studies following the 1967 Caracas earthquake, and was later confirmed both by laboratory tests and recordings obtained on "vertical arrays" with two or more accelerometric sensors at different depths within the same borehole. For instance, a statistical analysis of the numerous recordings of the Japanese KiKnet network [9] concluded that, for PGA (Peak Ground Acceleration) levels exceeding 0.75 m/s^2 (a rather moderate level) at an outcrop, there is a 40% chance of observing a non-linear soil response, leading to significant modifications with respect to the linear, low-strain response. These changes generally imply a reduction of the response amplification of the signal's high-frequency content and often a slight-to-significant increase of its low frequency content. Therefore, linear soil response estimates cannot be considered as being systematically on the safe side, and on the other hand, the high frequency reductions may significantly contribute to the safety margins. As a consequence, the accuracy, robustness and reliability of non-linear site effects directly impact the estimation of seismic hazard and associated risks, especially at long return periods.

While a consensus has undoubtedly been reached on the existence of non-linear effects, their quantification and modeling remains a challenge. Indeed, numerous techniques have been proposed for the assessment of site effects in the linear domain using empirical and/or modeling approaches on generic or site-specific basis. Conversely, empirical estimation of non-linear site effects is more limited, especially in moderate seismicity areas where the on-site instrumental approach can only be a long (to very long)-term investment. Aside from a generic approach based on existing recordings [10,11], the only presently possible way for site-specific estimates is thus numerical simulation. Obviously, such analysis must be precede by a precise geotechnical and geophysical characterization of the underground structure, and the choice of a suitable non-linear constitutive model.

Given the complexity of non-linear behavior of soils, many constitutive models and codes have been developed for such simulations. When the deformation remains moderate (i.e.,

smaller than about 0.1-0.3 %), the so-called "equivalent linear model", which is a linear approach with an iterative adjustment of visco-elastic properties (shear modulus and damping) to the local strain level, is often used and accepted in practice. However, when the strain level exceeds these values (i.e., above 0.2-0.5 %), which can occur in very soft soils and/or with very strong input motions, a complete non-linear modeling, with an appropriate constitutive law fed by the correct soil parameters is required. These models fall into two categories: relatively simple constitutive laws with few parameters, that cannot reproduce a wide range of loading/unloading paths; and more complex models with many parameters (sometimes exceeding 10), which can succeed in describing all possible behaviors, but with parameters that can be difficult to determine.

The ability to accurately predict non-linear site responses has indeed already been the subject of two recent comparative tests. It was one of the targets of the pioneering blind tests initiated in the late 80's/early 90's, on 2 sites of Ashigara Valley (Japan) and Turkey Flat (California); however, those sites lacked strong motion records until the 2004 Parkfield earthquake during which the Turkey Flat site experienced a 0.3g motion. Since the soils were fairly stiff, the nonlinearity was not very strong. A new benchmarking of 1D non-linear codes was thus carried out in the last decade, based on the Turkey Flat site and a few other sites with vertical array data (La Cienega, Caifornia; the KGWH02 KiK-net site in Japan, and Lotung in Taiwan). Its main findings, reported by Kwok et al. (2008) and in [12] emphasized the key importance of the way these codes are used and of the required in-situ measurements. Significant differences between records and predictions have been postulated as being due to an incorrect velocity profile (although it was derived from redundant borehole measurements), a non-1D soil geometry (non-planar layers), and imperfections / deficiencies in the constitutive models, which were unable to represent the actual curves for stiffness reduction and damping increase. Another test was undertaken on the Euroseistest European test site (Mygdonian graben near Thessaloniki, Greece) as part of the Cashima/E2VP project, which included two separate exercises on 2D non-linear numerical simulation codes and 3D, linear simulation codes. The 2D NL testing proved inconclusive, as major differences were found between the few considered codes, with multiple origins (2D numerical scheme, damping implementation, and NL constitutive laws (see [13]. Given the fact that the codes used for these tests are routinely used in engineering practice for predictions of non-linear site responses, especially for moderate seismicity countries lacking strong motion recordings, there is a clear need to conduct further tests in better controlled conditions, in particular with in situ and laboratory measurements for an optimal tuning of the non-linear parameters used in each code.

For this reason, the PRENOLIN project considers only 1D soil columns to test the non-linear codes in the simplest possible, though realistic, geometries. It is organized in two phases: (1) a verification phase aiming at a cross-code comparison on very simple (and "idealistic") 1D soil columns with prescribed linear and non-linear parameters; (2) a validation phase for comparison between numerical predictions and actual observations, for sites as close as possible to a 1D geometry (horizontal stratification), without liquefaction and with already available sets of downhole and surface recordings for weak and very strong motions and later complemented by careful in-situ and laboratory measurements designed as close as possible to the participants requirements. The sites were selected within the Japanese KiK-net and PARI (Port and Airport Research Institute) accelerometric networks.

The purpose of this article is to present and discuss the results of the verification phase, with a special focus on the epistemic uncertainties associated with the constitutive laws and numerical schemes of the simulation codes. The first section describes the 3 idealized soil

columns and the requested computations, considering different boundary conditions (rigid / elastic base, associated with within / outcropping reference motion). The next section lists the numerous teams that volunteered to participate in this exercise and the main characteristics of their codes. The simulation results are then presented and compared, first in the linear case (without and with attenuation), and then in the non-linear case for various input signals and levels, with a discussion in each case on the amount and origins of uncertainty.

2 The canonical cases

The verification phase of this project aims at establishing the similarity between the computed wave motions at the surface of a soil column affected by amplification using different numerical codes, quantifying the amount of code-to-code differences and, as much as possible, understanding them. When available, the computed responses were compared with predefined analytical solution when available. Figure 1 summarizes the calculations performed during the verification phase, for the linear (elastic and visco-elastic), and non-linear cases. In the elastic and visco-elastic cases, for which analytical results are available, similarity or even identity in the results is expected, provided that all participants/users share a common understanding of the physical soil parameters to be used; this is needed in order to ensure a proper predictability of the induced deformation (shear strain) for all soil and seismic wavefield properties. On the other hand, for non-linear cases, discrepancies between the different computations are expected: the goal is to identify their origins in relation to the constitutive models and/or the numerical schemes (or other possible issues), to quantify the associated epistemic uncertainty, and to reduce it to its minimum level as much as possible.

In order to do so, the experiment was designed around three 1D canonical cases, chosen to represent simple and idealistic soil conditions overlying hard bedrock substrata:

1) Profile 1 (P1) is a shallow (20 m thick), homogeneous soil layer presenting a significant velocity impedance ratio at rock, with amplification in the intermediate frequency range [2-10 Hz].

2) Profile 2 (P2) is a thick (100 m) soil layer with S-wave velocity gradually increasing with depth, overlying very hard bedrock, with a low fundamental frequency (below 1 Hz).

3) Profile 3 (P3) consists of two homogeneous layers with moderate velocity contrasts, overlying very hard bedrock, with amplification effects in the intermediate frequency range (2-10 Hz). The goal is to investigate non-linearity effects within both layers, since significant strains can develop at or near each interface.

Various reference motions are considered for each profile, from very simple signals intended to capture the basic physics of NL behavior (pulse like and cyclic, quasi-monochromatic signals with increasing amplitude), to realistic accelerograms: two were selected with very different spectral content (high and low frequency contents), and scaled to three PGA levels, in order to generate a wide range of shear strain levels in the soil column.

These reference motions were applied at the bedrock level, with two boundary conditions representative of the actual case studies: in one case, the reference motion was considered to mimic the outcropping motion as the surface of the underlying bedrock ("elastic" condition), while in the other it was considered to mimic the "within" motion recorded by a virtual sensor at the sediment-bedrock interface ("rigid" condition).

Figure 1 : The three simple idealized profile cases studied here (P1-3), for the elastic and non-elastic domains, and for a rigid and elastic soil-bedrock base, using a Ricker pulse and 3 accelerations of different PGA and frequency contents.

2.1 Soil properties

The properties describing the (1D) linear and non-linear soil behavior for each profile include elastic, visco-elastic and non-linear soil properties. They are displayed in Figure 1 and Figure 2, and summarized in Table 1.

The basic characteristics of soil profiles (i.e., thickness, density and seismic waves velocities) were chosen in order to be representative of typical soil profiles. V_P (P-waves velocity) values are derived from the V_S (S-waves velocity) profiles (shown in Figure 2), using assumed values of Poisson ratio (0.4 for soil and 0.3 for bedrock) Profiles P1 and P3 exhibit constant seismic velocities in each layer, while P2 includes a velocity gradient with a regular increase from Vs=150m/s at the surface to Vs=500m/s at the soil-bedrock interface, according to the dependence:

$$Vs(z) = Vs_1 + \left[\frac{(Vs_2 - Vs_1)(z - Z_1)}{Z_2 - Z_1}\right]^{\alpha}$$

Eq 1

where V_{S1} = 150 m/s and V_{S2} = 500m/s are the shear-wave velocities at depths Z_1 = 0 m and Z_2 = 100m, respectively, and $V_S(z)$ is the shear wave velocity at depth z; α is taken equal to 0.25.

2.1.1 Visco-elastic properties

We only consider intrinsic material damping [14–16], without any additional component from scattering. Intrinsic attenuation can be quantified by the quality factor Q (more commonly used in seismology), or the damping ratio ξ (used in engineering seismology). They are linked by the formula Q = 1/2ξ, and can be determined by the loss of energy over one wavelength. Pure elastic materials totally restore the seismic energy after (weak) deformation, and should therefore have infinite Q values; as the numerical codes used here required an input, as finite value as input, the "elastic" case was computed with very high values of Q (very low ξ) for both soil and bedrock (Q = 5000). For visco-elastic and non-linear (soft) materials, the energy dissipation at low strain was constrained to vary according to Vs, through the classical – never appropriately justified by measurements - relationship $Q_S = V_S/10$, or equivalently $\xi_S = 5/V_S$ (Vs in m/s) [17].

2.1.2 Non-linear soil properties

The non-linear properties of each layer were characterized using classical $G/G_{max}(\gamma)$ and $\xi(\gamma)$ curves, relating the decay of shear modulus (G) normalized by the elastic shear modulus (G_{max}) and increase of damping ξ with the shear strain γ. The $G/G_{max}(\gamma)$ and $D(\gamma)$ curves were constructed following a simple hyperbolic model based on the following equations:

$$K_0 = (1 - \sin(\phi)).OCR^{\sin(\phi)}$$

Eq 2

$$\sigma'_m = \sigma'_v(1+2K_0)/3$$

Eq 3

$$\tau_{max} = \sigma'_m \sin(\phi)$$

Eq 4

$$\gamma_{ref} = \tau_{max} / G_{max}$$

Eq 5

$$G / G_{max} = 1/(1+\gamma / \gamma_{ref})$$

Eq 6

$$\xi = \xi_{min} + (\xi_{max} - \xi_{min})(\gamma / \gamma_{ref}) /(1+\gamma / \gamma_{ref})$$

Eq 7

where the control parameters are the friction angle $\Phi = 30°$, the over-consolidation ratio OCR = 1 and the gravitational acceleration g = 9.81m/s^2. Only cohesionless material was considered here, so that the shear strength τ_{max} is mainly controlled by the vertical stress and the friction angle. σ_m' and σ'_v are the mean effective and vertical stresses; G_{max} is the maximum (low strain) shear modulus, γ is the shear strain, γ_{ref} the reference shear strain correspond to the strain for wich $G = 0.5G_{max}$ (in the hyperbolic model as describe above it is given by Eq 5), K_0 is the coefficient of earth pressure at rest, and ξ_{min} and ξ_{max} are the minimum and maximum damping values at very low strain (= intrinsic material damping considered above for the visco-elastic behavior), and at very high strain.

Only one $G/G_{max}(\gamma)$ and $\xi(\gamma)$ curves were provided for P1, five for P2 (increasing for each 20m depth interval), and two for P3 (one for each homogeneous layer). For all soil models we assume a constant strength per soil layer. They are illustrated in Figure 2. For P1 and P2, they are fitting a hyperbolic curve defined by the low strain shear modulus $G_{max} = \rho V_S^2$ and the shear strength τ_{max} at the center of each layer or sublayer. For P3 the $G/G_{max}(\gamma)$ and $\xi(\gamma)$ models chosen were very similar to one another using the previous hyperbolic model. For P3, the set of Darendeli models [18] was used and adjusted to a simple hyperbolic model as for P1 and P2; as Darendeli's models are defined only up to a maximum shear strain of 1%, the P3 curves were defined by multiplying the shear strength τ by factors 1.1 and 2 at depths of 10m and 35m, respectively, and the final curves were then computed based on the hyperbolic models associated to these values.

Some numerical codes include sophisticated constitutive models for NL soil behavior, which require very specific additional parameters, which should be consistent with the $G/G_{max}(\gamma)$ and $\xi(\gamma)$ curves supplied for the other codes. The definition of these additional parameters was done individually by each team, with the following simple assumptions: the soil is cohesionless (i.e. c' = 0 and Plasticity Index PI = 0), and the water table is located at 100m depth, the soil particle size distribution is defined with $D_{10} = 0.2$mm and $D_{50} = 0.35$mm, and a uniformity coefficient $= D_{60}/D_{10} = 1.8$.

Profile	LINEAR									NON-LIN-EAR
	Z [m]	**Vs** [m/s]	**Vp** [m/s]	**ρ** [kg/m^3]	**Q Elastic**	**ξ_{min} Elastic**	**Q Visco-Elastic**	**ξ_{min} Visco-Elastic**	**F_0 Linear Elastic** [Hz]	
P1	0-20	300	700	2000	5000	10^{-4}	30	0.0166	3.75	N°1-P1
	-	1000	1900	2500			200	0.0025		-
P2 *Mono-layer + $V_{gradient}$*	0-20	150-500	360-1220	2000			34	0.01547	1.16	N°1-P2
	20-40						40	0.0250		N°2-P2
	40-60						44	0.0113		N°3-P2
	60-80						47	0.0106		N°4-P2
	80-100						49	0.0102		N°5-P2
	-	2000	3700	2500			200	0.0025		-
P3 *Bi-layer*	0-20	300	700	2000			30	0.0166	1.48	N°1-P3
	20-100	600	1500	2000			60	0.0083		N°2-P3
	-	2000	3700	2500			200	0.0025		-

Table 1: Soil properties for all three simple profile cases studied here (P1-3), for the elastic and non-elastic domains.

Figure 2 : Vs profiles, G/G_{max} and damping curves for the 3 idealized profiles.

2.2 Reference rock motion

In the first phase of the project, each participant was provided (i) a simple Ricker pulse input motion derived analytically, and (ii) two real acceleration time histories scaled to three different PGA levels (0.5, 1 and 5 m/s^2) to observe the evolution from linear to non-linear soil behavior. The two accelerograms were selected to be representative of very different frequency contents, in order to analyze the influence of frequency in the non-linear computations. Each accelerogram was pre-processed in the same way as explained further below. The normalized Fourier transform of the three input motions are illustrated in Figure 3.

2.2.1 The pulse-like input motion

The Ricker pulse input motion corresponds to acceleration, velocity and displacement time-histories defined by equations (8 to 10). A central frequency of 4 Hz was chosen to produce sufficient energy at the fundamental frequency of each of the three profiles, while having a broad band energy in the main bandwidth of earthquake geotechnical engineering, i.e. 1 -10 Hz.

$$a(t) = \left[1 - 2(\pi t f_c)^2\right] \exp(-(\pi t f_c)^2)$$

Eq 8

$$v(t) = t \exp(-(\pi t f_c)^2)$$

Eq 9

$$d(t) = \exp(-(\pi t f_c)^2) / -2(\pi f_c)^2$$

Eq 10

where f_c is the central frequency and a(t), v(t) and d(t) are the acceleration, velocity and displacement time histories, respectively. The acceleration time histories and the normalized Fourier Transform spectra for the three input motions are illustrated in Figure 3.

2.2.2 Real reference input motions

To investigate the effect of frequency content on the computation of non-linear soil behavior, we used two real input motions with different frequency contents recorded at rock outcrop sites. One has a predominant frequency of 11.4 Hz, and the other of 4.8 Hz: they are labeled hereafter HF and LF, respectively. The metadata of these two recordings are described in Table 2 and their acceleration, velocity and displacement time histories are illustrated in Figure 3. We can observe that the spectral shape are quite different, the main energy of the signal for the LF motion lies between 0.5 to 10 Hz and for the HF motion between 5 to 20Hz. The duration of the HF event is about 80s while it is shorter for the LF motion around 15s. In this work, we considered only the horizontal EW component of each recording.

Event Freq. Content	**Event ID**	**Mw**	**Z** [km]	**Epi. Dist.** [km]	**Station ID**	**Station Geology**	**Seismo. Comp.**	**Vs30** [m/s]
HF	IWTH-170112022202	6.4	122	39	IWTH17 (Kik-net, Japan)	Rock	EW	>1200
LF	06756. 20000617	6.6	15	5	Flagbjarnarholt (Iceland)	A	H1	Unkno wn

Table 2: Seismic metadata of the two real input motions used in the verification phase of the Prenolin project.

The velocity and displacement time histories of these two recordings were calculated from the original raw acceleration data, following this procedure: (1) removal of the mean, (2) zero padding of the signal by applying Boore's approach [19] over a specific time period corresponding to 20s before the first, and after the last, zero-crossing of the original acceleration time series, (3) high-pass filtering of the signal, and (4) integrating twice to obtain consistent velocity and displacement time histories.

Figure 3: Normalized reference motion used for the verification phase of this project PRENOLIN.

3 Participants and tested numerical codes

We compared 23 different numerical codes used by 21 participating teams, as listed in Table 3. As some teams use several codes, each computational case/team is annotated by a letter and a number, Two or more teams used the same code, including Deepsoil (4 teams for the verification and 5 for the validation), Flac (2 teams) and OpenSees (3 teams). Others used the same constitutive model, notably Iai's (1990) model (3 teams) and the Hujeux model [20] (2 teams). The particpants teams teams were composed by people having different background and expertise. Firstly, two disciplines are represented in this bechmark, seismology and geotechnical earthquake engineering. Secondly, the participants are either developers or users. These differences are interesting when computing soil response.

We identified three different, non-exclusive code groups, according to three main characteristics: (1) the type of numerical scheme, (2) the way to implement the attenuation, either in the low strain range or in the large strain range, and (3) the type of non-linear constitutive models. Each of these three groups is detailed in the next sections.

Table 3: Participants to the PRENOLIN project Verification phase.

Team Name	**Affiliation**	**Team Index**		**Code Name**	***Code Reference***
D. Assimaki & J. Shi	***Georgia tech, US***	A	0	GEORGIA-NL-FDM	[21,22]
S. Iai	***DPRI, Japan***	B	0	FLIP	[23]
S. Kramer	***Univ. Washington, US***	C	0	PSNL	(In development)
E. Foerster	***CEA, France***	D	0	CYBERQUAKE	[24]
C. Gelis	***IRSN, France***	E	0	NOAH-2D	[23]
A.Giannakou	***Fugro, France***	F	0	DEEPSOIL 5.1	[25]
G. Gazetas E. Garini & N. Gerolymos	***NTUA, Greece***	G	0	NL-DYAS	[26,27]
J. Gingery	***UCSD, US***	H	0	OPENSEES-UCSD-SOIL-MODEL	(http://opensees.berkeley.edu/)
Y. Hashash & J. Harmon	***Univ, Illinois***	J	0	DEEPSOIL-NL 5.1	[25]
		J	1	DEEPSOIL-EL 5.1	[25]

P. Moczo, J.Kristek & A. Richterova	***CUB***	K	0	1DFD-NL-IM	…
S-Foti & S.Kontoe	***Politecnico di Torino & Imperial college, Italy***	L	1	ICFEP	(Grammatikopoulou et al., 2006; Kontoe, 2006; Taborda and Bielak, 2011)
		L	2	DEEPSOIL-NL 5.1	[25]
G. Lanzo, S. Suwal, A. Pagliaroli & L. Verrucci	***Univ. Rome La Sapienza, Italy***	M	0	FLAC_7,00	[31]
		M	1	DMOD2000	[32]
		M	2	DEEPSOIL 5.1	[25]
F. Lopez-Caballero & S.Montoya-Noguera	***ECP, France***	N	0	GEFDyn	[33]
F. De-Martin	***BRGM, France***	Q	0	EPISPEC1D	(Iai, 1990) http://efispec.free.fr
B.Jeremic, F. Pisanò & K. Watanabe	***UCD, TU Delft & Shimizu Corp, US***	R	0	real ESSI	http://sokocalo.engr.ucdavis.edu/~jeremic/PRENOLIN/
A. Nieto-Ferro	***EDF, France***	S	0	ASTER	http://www.code-aster.org
A. Chiaradonna, F.Silvestri & G.Tropeano	***UNICA and Univ. Naples, Italy***	T	0	SCOSSA_1,2	[34]
		T	1	STRATA	
MP. Santisi d'Avila	***UNS, Nice***	U	0	SWAP_3C	(d'Avila et al., 2012; Santisi d'Avila et al., 2013)
D. Mercerat	***CEREMA, France***	Y	0	GDNL	…
D.Boldini, A. Amorosi, A. Di Lernia & G. Falcone	***UNIBO and Politechnico di Bari***	Z	0	EERA	[37]
		Z	1	PLAXIS	[38]
M.Taiebat & P.Arduino	***Univ, Vancouver,***	W	0	Opensees	(http://opensees.berkeley.edu/)

3.1 *The numerical scheme*

The 20 codes that solve the problem in time domain are split in two main categories: two types of spatial approximations are considered:

(a) The Finite Element Method (FEM) is by far the most common, used by 18 teams and implemented in three different ways:
   i) Standard method (ST.FEM), used by 13 teams: B-0, D-0, H-0, L-1, L-2, M-1, N-0, R-0, S-0, T-0, U-0, W-0 and Z-1.
   ii) Spectral method (SP.FEM), used by 1 team: Q-0
   iii) Discontinuous Galerkin method (DG.FEM), used by 1 team: Y-0.

(b) The Finite Difference Method (FDM) is used by 9 teams: A-0, C-0, E-0, F-0, G-0, J-0, K-0, M-0 and M-2;

The last remaining teams (J-1, T-1 and Z-0) consider the problem in frequency domain and use a linear equivalent method (FrM) involving linear, visco-elastic material with several iterations to tune the visco-elastic properties in each layer to the shear strain and modulus reduction and damping curves [39].

3.2 Implementation of attenuation

Low strain attenuation: At low strain levels (less than 10^{-4}-10^{-2} %), elasto-plastic constitutive models have damping values close to zero, which is physically unrealistic, since all soils and rocks exhibit a hysteretic behavior in the stress-strain plane even for weak deformations, indicating dissipation of energy.

In the frequency domain, implementation of a prescribed attenuation factor is relatively straightforward. In theory, fulfillment of the causality principle leads to a (slight) frequency dependence of the shear wave velocity, which should be specified (together with the damping value) at a specific frequency f_0 [40] . However, this is not implemented in all codes: some consider a trully frequency-independent attenuation with a defined reference frequency for the velocity, while some dropped the causality principle and have frequency independent velocities.

In the time domain, attenuation can be approximated by implementation of a set of relaxation functions using rheological models such as the generalized Maxwell model [41–43,43,44] or modeled by a Rayleigh damping formulation. Both methods present pros and cons. The usage of rheological models to approximate attenuation is physical; however, adds memory constraints to the computations. The greater the number of relaxation functions used, the better the attenuation factor will be approximated (although one should not use too many (e.g. [45]. On the contrary, the Rayleigh damping method is much easier to be implemented numerically; nevertheless, the parameters are not easily determined, and automatically involve a significant frequency dependence of Q. At low attenuation (below a damping ratio of 20%) values (i.e., low damping ratio or high Q value), it was shown that Rayleigh damping and the generalized Maxwell model become equivalent [46].

For the entire set of codes tested here, four kinds of attenuation implementations were used:

(1) Frequency-independent attenuation (frIA): some considered in the time domain analysis by the use of series of Maxwell/Zener elements Blanch et al., 1995; Day and Bradley, 2001; Day and Minster, 1984, 1984; Graves and Day, 2003), which imply an almost constant attenuation over a specific, broad enough frequency range, others frequency independent attenuation as proposed in[47]. Nine teams used this attenuation model: A-0, E-0, F-0, J-0, K-0, J-0, M-2, Q-0, T-1 and Z-0.
(2) Frequency-dependent attenuation (frDA), such as the Rayleigh damping (simplified or full). It was used by 10 teams: B-0, G-0, H-0, L-1, M-0, M-1, R-0, S-0, T-0, W-0, Y-0 and Z-1.
(3) Low strain frequency independent hysteretic damping (LSHD). It was used by 4 teams: C-0, N-0, D-0 and R-0.
(4) Numerical damping (ND). 3 teams (U-0, N-0 and D-0) use the Newmark integration method to simulate attenuation effects with purely numerical damping tools, while another team (L-1) used it to filter out numerical noise (NDfilt).

High strain attenuation: High strain attenuation can be computed directly from the hysteretic behavior of the soil subjected to strong ground motion (loading / unloading cycles).

However, it was demonstrated it is difficult to reproduce simultaneously the specified decrease of G/G_{max} with increasing shear strain, and the increasing of damping. For this reason, a few teams (A-0, B-0, E-0, J-0 and T-0) chose to use a "damping control" (which implies a modifcation of the "Masing rules, and is thus labeled as 'no-Masing rules'): it is based on a mapping that converts a hysteresis loop in such a way that it will satisfy the hysteretic damping at the current strain level [48]. These changes cause modification of the loading and unloading paths changing the G_{max} after unloading at large strains. Indeed, this question is not solved yet.

3.3 Non-linear constitutive models

In geotechnical earthquake engineering, non-linear soil behavior is a well-established concept. In laboratory experiments, such as cyclic tri-axial tests, the non-linear soil behavior is expressed by hysteresis loops in axial stress-strain plots, which can be linked to shear stress-strain plots. The soil response under cyclic loading (representing seismic loading) depends on the properties of the cyclic loading (time history, peak amplitude, etc) and on the soil properties (strength, relative density…).

In non-linear models, the true hysteresis soil behavior is simulated by the use of constitutive models which mimic the experimental hysteresis curves, or the shear modulus decay ($G/G_{max}(\gamma)$) and attenuation ($\xi(\gamma)$) curves.

According to information gathered from each participant, the codes tested here are implemented with various non-linear models, including:

⇒ Iai model [49,50]: B-0, E-0, Q-0,

⇒ MKZ modified hyperbolic model [22,51]: A-0, T-0

⇒ Cundall's model [52]: M-0

⇒ Iwan's model [53,54]: K-0,U-0, Y-0

⇒ Logarithmic function model [55] : L-1

⇒ Modified Hujeux model (Aubry et al., 1982): D-0, N-0

⇒ Multiyield model (Elgamal et al., 2003; Yang et al., 2003): H-0

⇒ Extended Hyperbolic model(Phillips and Hashash, 2009b) : F-0, H-0, J-0, M-2

⇒ HSsmall (Isotropic hardening elasto-plastic soil model) (Schanz et al., 1999): Z-1

⇒ Elasto-plastic (Pisanò and Jeremić, 2014): R-0;

⇒ BWGG: Extented Bouc Wen model (Gerolymos and Gazetas, 2005): G-0

⇒ Modified extended hyperbolic model: C-0

⇒ Manzari-Dafalias model: W-0 (Dafalias and Manzari, 2004)

In order to compare the different constitutive models, stress/strain controlled tests could have been conducted. However, some of the teams were not able to perform it. To overcome this difficulty, we asked the teams to compute nonlinear simulations with their codes on one of the idealized soil profile (P1) with a sinus input motion and with a rigid substratum base (Figure

4). The frequency of the input motion being low enough to avoid any issues with wave propagation. Moreover, the result of such simulation was asked at the node before the soil/bedrock interface, having a strength of 65 kPa.

The resulting plots are illustrated in Figure 5 for the total length of motion and in Figure 6 for a specific zoom on the first two cycles (blue for the first and red for the second).

The full duration of motion leads to very high strain levels (5%), and the stress-strain curves are highly variable from one computation to another. Even for a similar constitutive model, the curves can differ a lot depending on the use or not of damping control. For instance, teams B-0, E-0 and Q-0 used Iai's model, however their computational results are clearly different, as teams B-0 and E-0 used damping control, and the other did not.

Some teams could not follow the prescribed shear strength values (F-0, M-0, M-1, M-2, R-0, S-0) mainly because of depth dependency of the shear strength implemented in the code. They used very different values; the comparison of the corresponding stress-strain curve is thus irrelevant. Therefore, we looked at the first two cycles of motion that involve much lower strain (not exceeding 0.5%): the stress-strain curves are closer to each another although some indicate larger hysteresis loop (B-1) and others indicate a low strain shear modulus much lower than expected (Z-1 and F-0). This comparison helped to draw the attention on the lack of versatility of some of the used NL codes, because of some built-in features based on empirical correlations or geotechnical relations (between the shear strength and the confining pressure, for instance), which prevent from considering fully arbitrary sets of NL parameters.

Figure 4 : *Acceleration time history of the sinus motion with central 1s period*

Figure 5 : *Stress-strain curve for a soil element of shear strength 65kPa subjected to a sinusoidal input seismic motion of 10s.*

Figure 6 : *Stress-strain curve for a soil element of shear strength 65kPa subjected to the first two cycles of a sinusoidal input seismic motion.*

3.4 Code usage protocols

Reference frequency for visco-elastic damping

Relatively little is known about low-strain, intrinsic attenuation in real soils. Its traditional implementation supposes frequency independent damping values. This is readily achieved using the Kelvin-Voigt model when solving the wave propagation in the frequency domain (Ishihara, 1996). Conversely, the Maxwell/Zener generalized body better describes inelastic material properties in both the time and frequency domain solution of wave propagation (Moczo et al., 2004). However, the use of this rheology implies a slight velocity dispersion to fulfill the causality principle. It is therefore needed to carefully define a reference frequency for the reference velocity value, especially when different numerical methods are compared with one another (Peyrusse et al., 2014). *[This reference frequency must not be confused with the frequency bandwidth definition of the quasi-constant Q value used in the frequency independent attenuation method aforementioned, it should simply be within this frequency bandwidth.]*

A reference frequency was thus defined for each profile, at which common velocity and attenuation values were fixed. As indicated by some authors (Liu and Archuleta, 2006; Moczo et al., 2004) the values of reference frequency used in most cases is close to 1 Hz (as many 3D computations including shallow, soft material, have rather low upper bound maximum frequencies). On the other hand, it is often suggested to select a frequency close to the

frequency of interest. In our case, given the definition of the pulse-like motion, we chose a reference frequency of 4 Hz, i.e. the central value of the input wavelet.

Definition and implementation of the reference motion

We tested two base conditions at the sediment-substratum interface: (i) an elastic base, and (ii) a rigid base. The first condition corresponds to the usual hazard assessment studies, where the rock ground motion is derived from deterministic or probabilistic analysis, and corresponds to the design motion at the surface of an outcropping rock. The second one corresponds to the case where a recording is obtained at depth within a down-hole array, and is used to derive the motion at surface or shallower depths. Depending on the communities or point of views, the implementation of input (or reference) motions into algorithms can be quite different, indicating that the terms "input motion" or "reference motion" are not understood in the same way by all the participants. For the seismological community, the input motion is often seen as the seismic signal carried by the up-going incident wave, while for the geotechnical community, it is often understood as the motion at a given reference rock site, resulting from the total-wavefield (up-going and down-going waves): this reference site may be either at rock surface, (it then includes the free-surface effect), or at depth (for instance the downhole sensor of a vertical array, which includes the interferences between the up-going and down-going waves).

For the case of a perfectly rigid substratum, the reference input motion is the signal imposed at the soil-bedrock interface. This definition was clear among all teams. It was not so clear for the elastic substratum condition, whereby a more precise definition was required, since the greatest differences in the first round results came from different understandings of the term "input motion" by the various teams. The terminology must therefore be clearly stated:

- Outcrop motion: Seismic motion recorded at the surface and corresponding to free surface conditions in the outcropping rock. For 1-D cases, with vertically propagating seismic waves and homogeneous rock, this free-surface effect is simply a frequency-independent factor of 2, with respect to the up-going wave signal.

- Surface motion: Seismic motion recorded at the free surface of a sedimentary site and subjected to amplification effects.

- Within motion: Seismic motion recorded at depth, usually at a downhole site: in our case, this location corresponds to the interface between sediment and rock substratum (i.e., z=20, 100 and 50 m, for profiles P1, P2 and P3, respectively). This motion contains the total wave-field composed of the incident up-going and reflected down-going waves.

- Incident motion: Seismic motion that is carried by the incoming waves just before they enter the sedimentary filling. In our case, it is the seismic motion carried by the vertically incident plane wave, and it cannot be measured directly.

Considering the confusion among the participants linked with different working traditions in different communities, we decided to use the concepts of “outcrop” and “within” input motions to define the "reference motion" at the downhole sensor, as recommended by Kwok et al. (2008) and Stewart and Kwok (2009). In linear/equivalent linear/non-linear site response analyses, two cases can be distinguished:

(1) if the reference motion is an outcrop recording, then one should use an elastic base condition with an up-going wave carrying a signal equal to exactly half the outcropping motion;

(2) if the reference motion is a within motion recorded by a downhole sensor, then one should use a rigid base condition without modifying the input motion.

In order to avoid any ambiguity, we will systematically use the expression "reference motion" which should be understood as detailed above for the elastic and rigid base conditions

4 Comparison of predictions

4.1 Methodology of comparison

The participants were asked to compute the acceleration and stress-strain time histories at virtual sensors located at different depths within the soil profile. A total of ten virtual sensors were selected for each profile, with a depth interval equal to 1/10th of the total soil thickness: every 2m for P1, every 10m for P2 and every 5m for P3. Acceleration and (stress, strain) should be computed at staggered points: from the very surface for acceleration, and from half the depth interval for stress-strain values.

From the "raw" results provided by each participant, a comparative analysis was performed on the computed acceleration time histories, transfer function, 5% pseudo-response spectra, the depth distribution of peak shear strain and PGA, and the stress-strain plots at different depths. Such comparisons were done for each profile, for each computational case (linear vs. non-linear, elastic vs. visco-elastic soil behavior, and rigid vs. elastic substratum conditions) and for the different input motions.

For the sake of simplicity and conciseness, the main section of the present article presents results for only the P1 case. Some additional plots may be found in the electronic supplement. The P2 and P3 profiles are compared to P1 results in terms of variability of the surface motion only, but the conclusions are based on the consistent results from all three profiles.

4.2 Visco-elastic computations

Figure 7 displays the comparison for the P1 profile of the surface acceleration for the pulse-like motion under an elastic substratum condition, for the linear elastic computation for a short window (3 s) of signal. All results converged towards the analytical solution calculated with the Haskell-Thomson method (Thomson, 1950; Haskell, 1953), but this was achieved only after the second iteration. There were indeed unexpected and significant discrepancies in amplitude at the end of the first iteration, and that came from: (1) inconsistent implementation and understanding of the term "input motion" (clarified as mentioned in the code usage protocols), (2) problems with units, or (3) representations of soil properties. During the first iteration, some motion phase discrepancies could be identified also, associated either to the assignment of the "input motion" at different depths some distance below the sediment/rock interface (which caused a constant time delay), or to increasing time delays for the late cycles, that were associated to numerical dispersion.

***Figure** 7: Comparison of the acceleration at the surface of P1 profile, for the pulse-like input motion, for the linear elastic computation and for the elastic substratum case.*

Figure 8 shows the results of visco-elastic computations of the acceleration at the surface of the pulse-like motion with a rigid substratum condition. The convergence was also obtained after the second iteration, with minor corrections (similar to the ones observed for the elastic case) and after having specified the reference frequency to be considered for the

implementation of damping. We chose a reference frequency of 4Hz, which is exactly the central frequency of the pulse-like motion (Figure 8).

Figure 8 *Comparison of the acceleration at the surface of P1 profile, for the pulse-like input motion, for the linear visco-elastic computation and for the rigid substratum case.*

These unexpected issues were corrected after the first iteration to ensure a satisfactory convergence. This should however raise our awareness on the possibility of such misunderstandings and resulting errors, when site response computations are asked without clear enough specifications about the definition of the reference motion.

4.3 Non-linear computations

Once agreement between the model predictions was reached for simple, linear cases for which analytical solutions are available, the variability of the results of non-linear calculations can be fully associated with differences in implementation of non-linear soil behavior.

Figure 9 compares the Fourier transfer functions (surface over reference bedrock motion) and Figure 10 compares pseudo-response spectra at the surface for the P1 profile, with a rigid substratum case. The subplots of these two figures illustrate the results for the high frequency (HF) waveform scaled to the lowest (0.5 m/s^2) and largest PGA (5 m/s^2) (a and c, respectively), and for the low frequency (LF) waveform scaled to the lowest and largest PGA (0.5 m/s^2 – b, and 5 m/s^2, d, respectively). The frequency content of the input motion and the scaling of the input motion prove to have a large influence on the non-linear soil behavior in the numerical simulations, and consequently on the dispersion of the results.

While the results from all teams exhibit a very satisfactory similarity (though larger than for the visco-elastic case) for the HF waveform scaled to the lowest PGA (a), differences between the model predictions are much greater the highest PGA (c). This observation is more pronounced when looking at the LF input motion. Even for the lowest PGA (b), the variability increases significantly compared to the HF input motion, and it becomes very large for the large amplitude LF motion (scaled to 5 m/s^2, d).

The amount of variability between the results has been quantified through the calculation of the standard deviation (in log10 unit) for each frequency value is illustrated in Figure 11. The variability is greater for the low frequency content input motion scaled to the highest PGA except close to the first frequency peak of the linear transfer function. As expected, strong non-linear soil behavior during this solicitation shifts the first frequency peak of the transfer function to the low frequency content. The variability of the transfer function is similarly shifted.

Such variability is strongly linked to the peak shear strain reached in the soil column. For the LF input motion scaled to the highest PGA, the threshold shear strain above which the numerical simulations can no longer be considered as reliable (according to their authors), was reached by some codes. Indeed, some codes consider a maximal reliable deformation between 1 to 2% (L-0, Z-0); while others consider their code to work well over a wide range of deformation and are limited by the dynamic soil properties resolution only. For the computations using the HF and LF motions scaled to the highest PGA, we observe that the two equivalent linear methods (J-1 and Z-0) exhibit a very higher de-amplification beyond 7 Hz, compared to the other simulations, which shows the classical over-damping limitation of that method. For the last two cases (HF and LF accelerograms scaled to 5 m/s^2), the peak shear strain values are illustrated in Figure 12. It was calculated for each code/team couple, and for all the 10 sensor depths of the P1 profile. The largest peak strain values, largely

exceeding 1%, are reached at the deepest points for the LF input motion, while it remains about 10 times smaller (max 0.3%) for the HF motion, despite the identical PGA values on the input motion. Besides, given the shape of the G/G_{max} and $\xi(\gamma)$ curves, one may notice that the frequency-content of the input motion induced variability in the peak shear strain results which correspond to an even larger variability in the G/G_{max} and $\xi(\gamma)$ values. For instance, at 7m depth, the peak shear strain for the LF motion is between 0.02 to 1% while it is between 0.03 to 0.1% for the HF motion. This makes the G/G_{max} varies from 0.28 for the LF motion to 0.8 for the HF motion. Thus, one may understand that the results will be very sensitive to the details of the constitutive model and the way that G/G_{max} and $\xi(\gamma)$ curves are approximated.

Incidentally, one may also notice that for P1, the peak shear strain occurs at the deepest point, close to the sediment/bedrock interface. Indeed, wave propagation in nonlinear media is the cumulative effect of impedance contrast at the soil-bedrock interface, material strength, and intensity of the input motion. These combined effects make it uneasy to analyze these results even when they are numerical and consider simple soil geometry.

Figure 9 : Comparison of the surface to reference Fourier spectra ratio, for the non-linear comparison using for the left sub-graphs the high frequency input motion and for the right sub-graphs the low-frequency input motion and with for the first line the weakest input motion PGA and the second line the highest input motion PGA.

Figure 10 : Comparison of the acceleration pseudo-response spectra at the ground surface, for the non-linear computation using for the left sub-graphs the high frequency input motion and for the right sub-graphs the low-frequency input motion and with for the first line the weakest input motion PGA and the second line the highest input motion PGA

Figure 11 : Standard deviation (in log unit) of the transfer function (left panel) and response spectra (right panel) depending of the input motion used.

Figure 12 : Peak shear strain profiles reached at each depth by each team for the high and low frequency reference motion scaled at the highest PGA level (5 m/s^2), for the profile 1 and for rigid substratum conditions

5 Epistemic uncertainty

5.1 Quantification of result variability

We quantified the variability between the simulations by the standard deviations (log10 units) of several ground motion intensity parameters, starting with PGA values [σ_{PGA}], and then considering spectral ordinates at different periods [$\sigma_{PSA(T)}$], peak strains [$\sigma_{\gamma max}$], and a few energy related quantities.

The PGA values at the surface are first compared with the empirical variability (i.e. single station, within-event variability "Φ_{SS}"). Figure 13 illustrates the evolution of σ_{PGA} for the surface site of P1 for the 5 different computational cases and the different reference motion and boundary conditions. These are the linear–elastic, the linear-visco-elastic, and the non-linear computations with the input motions scaled to the lowest (0.5m/s^2), intermediate (1m/s^2) and highest (5m/s^2) PGA. The σ_{PGA} is calculated for the pulse-like, the HF and the LF motions. The left subplot displays the results for the rigid substratum case (reference motion = within motion at sediment-basement interface), while the right subplot stands for the elastic substratum case (reference motion = outcropping rock motion). The most striking features of these plots can be summarized as follows:

a) the (almost) systematic increase of σ_{PGA} with increasing PGA level, whatever the input signal and the type of boundary conditions

b) the (almost) systematically larger values of σ_{PGA} for the LF input motion compared to the HF input motion case (around twice greater for the three PGA values) : this corresponds to the higher strains generated by the LF motion. A similar plot as a function of peak strain instead of peak ground acceleration would exhibit a larger continuity between results of both input waveforms
c) the larger σ_{PGA} values for non-linear computations compared to the linear case (except for the very specific case of linear-elastic response with rigid boundary conditions, discussed later)
d) the maximum obtained σ_{PGA} value (0.15) remains below the specific single-station, within-event variability $\Phi_{SS,PGA}$ value for a site with a V_{S30} equivalent to P1 (Rodriguez-Marek et al., 2011), which is around 0.2. The uncertainties linked with the NL simulations remain below the "natural" single site response variability. The latter one however includes the sensitivity to the characteristics of the incident wavefield, which is not accounted for here as only vertically incident plane waves are considered. Nonetheless, the use PGA as a main metric is not enough. It is helpful to use spectral accelerations at other periods as well.

Our results indicate an exceptionally high σ_{PGA} value for one linear computation, the linear-elastic one with the HF reference motion and rigid boundary conditions. This computational case is the simplest but also the most demanding for a propagating seismic wave. Considering that no seismic attenuation (damping) is considered for this specific computation (in the material or in the substratum), some codes usually use numerical attenuation to control real motion amplitudes. Thus, the high uncertainty observed here reflects variability in the implementation of the numerical damping for each code/team couple, together with the high sensitivity to the configuration, with a non-zero Fourier content of the reference motion at depth, at a frequency where destructive interferences between up-going and down-going waves should result in a null motion.

Figure 13 : Standard deviation (in log10 unit) of the PGA at the surface of the P1 profile, for the 5 different computational cases (linear –elastic, linear visco-elastic, non-linear with input motion scaled to the lowest (0.5m/s^2), medium (1m/s^2) and highest (5m/s^2) PGA, for the pulse-like, the high frequency and the low frequency content motions. The left sub-plot shows the results for the rigid substratum case and the right sub-plot for the elastic substratum.

We then explored the variability of various seismic intensity measures: (i) the response spectra at the surface at three different periods (0.1, 1 and 3s), (ii) the peak shear strain at the bottom of the sediment layer (ε), (iii) the Cumulative Absolute Velocity (CAV), (iv) the Arias Intensity (IA), (v) the root mean square acceleration (Arms), and (vi) the 5%-95% Trifunac-Brady duration (DT). The tendencies are quite similar for the HF and LF motions, but are sensitive to the sediment/substratum limit condition (elastic vs. rigid). Considering that σ_{PGA} is greater for the LF motion, we choose that motion to illustrate the results in Figure 14.

For the rigid substratum case (left subplot), three groups of intensity parameters can be identified. The first group is composed of duration-dependent intensity parameters, i.e., CAV, IA and DT, which exhibit the largest σ values. The second group is composed of acceleration parameters (PGA, SA(T), Arms) and characterized by a lower σ, especially for long period [SA (T = 1 s)]. The third group consists only of the peak strain, with generally intermediate σ values, which however exhibit the largest variability form one case to another. These three groups can also be distinguished in the elastic substratum case (right subplot), for which the largest case-to-case variability is also observed for the peak strain, exhibiting the highest σ for the highest PGA values. The duration-dependent parameters of group 1 are less variable under elastic boundary conditions especially at low to intermediate PGA levels and in the linear

domain: rigid base conditions are very demanding for low damping materials, which maps much more on duration than on peak values.

Figure 14 : Standard deviation (in log unit) of the different intensity parameters for the P1 profile, for the 5 different computational cases (linear –elastic, linear visco-elastic, non-linear with input motion scaled to the lowest (0.5m/s^2), medium (1m/s^2) and highest (5m/s^2) PGA, for the low frequency content motion. The left sub-graph shows the results for the rigid substratum case and the right sub-graph for the elastic substratum.

The other profiles provided similar results as to the variability of predictions. As an example, Figure 15 compares the PGA variability, for the LF motion and a rigid substratum case, for the three profiles. The trends are similar for the three profiles: similar σ values, same tendency to increase with PGA. These results also stand for the elastic substratum case, as well as the fact that the variability σ is lower for the HF motion for the three profiles, by about a factor of two compared to the LF motion.

Figure 15 : Standard deviation (in log unit) of the PGA for the profile 1 2 and 3, for the 5 different computational cases (linear –elastic, linear visco-elastic, non-linear with input motion scaled to the lowest (0.5m/s^2), medium (1m/s^2) and highest (5m/s^2) PGA, for the low frequency content motion and for the rigid substratum case.

5.2 Origins of the variability: Can it be reduced?

Definition of Groups and Sub-groups

We considered four a priori ways to group the results according to some characteristics of the numerical codes: (G1) implemented attenuation method, (G2) numerical scheme, (G3) constitutive model, (G4) shape of the hysteretic curve according to (1) the ability to represent the actual shear strength value (here at the bottom of P1), and (2) the use or not of Masing rules for the loading/unloading path (damping control or not). Each group is further sorted into several sub-groups as follows.

Case G1 concerns the implementation of linear, intrinsic damping, as defined in the first part of this article. It is sub-divided into 3 sub-groups: (i) G1a: frequency-independent attenuation (A-0, E-0, F-0, J-0, J-1, K-0, M-0, Q-0 and Z-0), (ii) G1b: Rayleigh damping (B-0, G-0, H-0, L-1, M-1, R-0, S-0, T-0, W-0, Y-0 and Z-1), and (iii) G1c: low strain hysteretic damping (C-0, N-0, D-0 and R-0).

Case G2 is based on the numerical discretization scheme, which is sub-divided into 2 subgroups: (i) G2a: finite-element (B-0, D-0, F-0, H-0, J-0, L-1, M-0, M-2, N-0, Q-0, R-0, S-0, T-0, U-0, W-0, Y-0 and Z-1), and (ii) G2b: finite-difference (A-0, C-0, E-0, G-0 and K-0). A third sub-group could be considered G2c: consisting of equivalent linear codes working in the frequency domain method (J-1 and Z-0).

Case G3 is based on the constitutive model. To ensure sufficient teams within each group, we split the code/team couple into 4 sub-groups according to the main constitutive model used: (i) G3a: IaI's model (B-0, E-0, Q-0), (ii) G3b: Iwan's model (K-0, L-1, U-0, Y-0), (iii) G3c: Philips and Hashash's model (F-0, J-O, M-2, T-0), and (iv) G3d: all other models.

Case G4 is based on the shape of the hysteresis loop according to (1) the shear strength used by each code/team couple and (2) the use of Masing rules or not for the loading/unloading path.

In the "canonical" models initially designed by the organizing team, the soil shear strength profile was assume to be constant with depth in each soil layer, and had prescribed modulus reduction and damping curves. However, in most real situations, the shear strength should

increase with depth. Even though these profiles were considered as "idealized" and simply intended to perform these verification tests, some teams felt very uncomfortable with this unrealistic assumption and decided to change the shear strength profile, by introducing a more realistic increase in shear strength with depth, having nevertheless, the imposed strength values at the center of each layer. Consequently, the actual non-linear soil parameters considered by each team were not identical, which is certainly responsible for part of the final variability observed, especially for large ground motions, for which the actual strain and damping are more sensitive to the shear strength than to the shear velocity, particularly at or close to major interfaces. For this reason, we further sorted each code/team couple into 2 sub-groups, by analyzing the stress-strain plots for the LF motion and the highest PGA at the bottom of P1 (illustrated in Figure 16): (i) shear strength is equal to 65kPa, as stated by the organizing team (A-0, B-0, C-0, E-0, F-0, G-0, H-0, K-0, Q-0, U-0, T-0, Y-0), and (ii) all others that exceeded this value (D-0, J-0, J-1, L-1, N-0, M-0, M-1, M-2, R-0, S-0, W-0, Z-0, Z-1).

In addition, we also consider the damping control implementation, (or in other words the use or not of the Masing loading/unloading rules). It has a major influence on the hysteresis curves and hence on the non-linear soil behavior, also illustrated in Figure 16. It is split into 2 sub-groups: (i) damping control is used, i.e. the Masing rules are not applied (A-0, B-0, E-0, F-0, J-0, M-2), and (ii) no damping control used (all other teams).

Combining these two last parameters we end-up for G4 with three subgroups as follow: (i) G4-a: Specified shear strength and use of damping control (A-0, B-0, E-0, F-0), (ii) G4-b: Specified shear strength and no use of damping control and (C-0, G-0, H-0, K-0, Q-0, T-0, U-0, Y-0) (iii) G4-c: Different shear strength (D-0, J-0, J-1, L-1, N-0, M-0, M-1, M-2, R-0, S-0, W-0, Z-0, Z-1).

Figure 16 : Stress-strain curves at the bottom of P1 Profile for the Rigid substratum case subjected to the low frequency motion (in color and the high frequency motion in black scaled to the highest PGA (5m/s2). The grey curves are for code/team couples that exceed the specified shear strength of 65 KPa, whereas the coloured curves represent the code/team couples that use 65 KPa. The blue curves are for codes using damping control and the red curves the others.

5.2.1 Variability within the sub-groups

Considering the level of code-to-code variability, and its increase with PGA or strain level, a major issue regarding non-linear computations is whether such variability, i.e. the uncertainty in the predicted motion, is intrinsic to these kinds of calculations, or can be reduced, and in the latter case, how? We thus looked at the variability within each subgroup of the 5 main grouping, in order to identify those, which are associated to a significantly reduced scatter.

The standard deviations (σ_{log}, calculated in log_{10} units) of three parameters describing the computed surface accelerations and the strain levels at the bottom of P1, were used as a metrics to validate the ability of a given grouping item to reduce the scatter of results. These parameters are the surface PGA and the acceleration response spectra (RS) at periods 0.3 s and 0.09 s (corresponding to P1's first and second resonance frequencies, respectively). For each, the variability was measured within each subgroup of the 4 groups. If the groupings are physically relevant, the within-subgroup variability should be significantly reduced.

Figure 17 shows the standard deviation values for each sub-group in each group (G-1, G-2, G-3 and G-4) relative to the general standard deviation (all unsorted code/team couples) illustrated by the dotted gray line. The standard deviation of the PGA, response spectra at two periods and maximal deformation are calculated on the results for the profile P1, with the

rigid substratum case and using the low frequency input motion scaled to the highest PGA (i.e. the motion that induces the strongest deformation in the soil column).

G1 and G2 (i.e. low strain attenuation and numerical scheme implementation, respectively) do not exhibit much lower σ_{log} values compared to the general σ_{log}, except for the lowest PGA input motion. Conversely, G4 to G5 (i.e. constitutive model, shear strength and damping control groups) do show reduced σ_{log} relative to the general σ_{log}, with G4 demonstrating the strongest reductions (by at least a factor of 2).

We can therefore conclude that (i) the shear strength is a key parameter for non-linear computations, and (ii) the constitutive model has a large influence; however (iii) the use (or not) of Masing rules appears to have an even greater influence for really strong input motion.

Figure 17 : Standard deviation values (σ_{log}, in log_{10} units) of four parameters for the non-linear computation using the low-frequency content input motion scaled to the highest PGA : PGA (upper left), Response spectra at 0.27 s (upper right), Response spectra at 0.09 s (lower left) all three at the surface of P1 and the maximal shear deformation at the bottom of the P1 profile (lower right). The standard deviation are given for each group of the four groupings: depending on their low strain attenuation implementation (G-1) their numerical scheme (G-2) their constitutive models (G-3) and their values of shear strength at the bottom of P1 and use of damping control or not (G-5). The grey area illustrates the standard deviation for all code/team couples.

Figure 18 compares the pseudo-acceleration response spectra at the surface of the P1 profile with a rigid substratum condition subjected to LF and HF input motions scaled at the medium ($1m/s^2$) and highest ($5m/s^2$) PGA levels. The response spectra are sorted according to the G4 sub-grouping, and the associated σ_{log} is represented by the thin lines on top of each subplot (the numbers on the right side indicate the number of code/team pairs in each sub-group). G4 enables a clear distinction of the response spectra; particularly for the most demanding LF input motion. The σ_{log} values from the two sub-groups with identical τ_{max} (G4a and G4b)- are considerably reduced below 2s, compared to the rest of the computations (G4c). This period bandwidth is relative to the PGA of this LF input motion. Similarly, for the HF input motion, the σ is reduced below 1s.

Figure 18 : Comparison of the pseudo- acceleration response spectra at the ground surface of P1 with rigid substratum condition, for the non-linear computation using for the left sub-graphs the high frequency input motion and for the right sub-graphs the low-frequency input motion and with for the first line the middle input motion PGA and the second line the highest input motion PGA. The response spectra were sorted according to three groups: group 1 is composed of the code/team couples using similar τ_{max} and damping control constitutive model. Group 2 use similar τ_{max} and no damping control and Group 3 are the other code team couples.

The team E-0 performed additional tests on their numerical method, with and without damping control. Figure 19 displays the comparison in the stress-strain curves at the center of P1 (z = 10 m), and Figure 20 illustrates the same comparison but in terms of the ground acceleration time histories at the surface for the LF input motion scaled at the highest PGA ($5m/s^2$). The stress-strain behavior from the damping control case is inconsistent with laboratory testing. While such method gives better results at high strain, it seems to do so at the expense of accurate stress-strain curves. For this input motion that generates high strain in the soil, the damping control has a large influence on the results, even when the same non-linear constitutive models with the same parameters are implemented.

Figure 19 : Comparison of the stress-strain curve at the middle point of P1 for the low frequency reference motion scaled at the highest PGA level ($5 m/s^2$) and for E-0 team with and without damping control.

Figure 20 : Comparison of the acceleration time history at the surface for the low frequency reference motion scaled at the highest PGA level ($5 m/s^2$) and for E-0 team with and without damping control.

6 Conclusions

In the PRENOLIN's verification phase, the linear computation involving a simple pulse-like (Ricker) input motion proved to be very useful in understanding and eliminating some of the discrepancies between the different numerical codes that were compared. It was found that code-to-code differences can be attributed to three different sources: (1) minor mistakes in input parameter implementation or output units, (2) different understanding of the expression "input motion" within different communities, and (3) different intrinsic attenuation and numerical integration implementations. This benchmark showed that any nonlinear code should be tested with simple linear cases before going into nonlinear computations to ensure the proper implementation of the elastic soil parameters.

Most of the codes tested in this verification benchmark were designed mainly for non-linear computations. Therefore, although the codes should well reproduce the soil behavior at low strains, their actual performance are mainly tested for their soil behavior predictions during strong shaking in real cases.

The results obtained so far indicate a code-to-code variability, which increases with the shear strain level (which in turn depends on both the PGA level, stiffness of the soil and the frequency content of the reference input motion). We also found that, whatever the soil profiles used (among the 3 soil profiles considered), the overall code-to-code variability in the worst case (with strain levels exceeding 1%) remained lower than the random variability of GMPE single-station σ values for PGA. Nevertheless, an important conclusion is that given the scatter in the nonlinear results, a realistic analysis should use more than one code to perform a site response computation.

The effect of different non-linear soil model implementations was explored in this study and our main observations indicate that the epistemic uncertainty (i.e. the code-to-code variability) can be significantly reduced by describing more precisely some specific input parameters, especially the soil shear strength profile, which is found to be a key specification in addition to the degradation curves. In addition, for one particular non-linear soil model implemented in different codes (Iai's model), the variability of the stress-strain curves were found to be large, and mainly caused by the damping control parameter, depending on whether it was used to simultaneously fit the strain-dependence of both shear modulus and damping, or not, in order to follow the Masing loading/unloading rules. All these features and conclusions need to be checked against actual data to provide support for defining best practice for modeling out of the many available: vertical arrays with multiple down-hole sensors are the best available in-situ instrumentations to go forward. The bennhnmak undoubtedly benefits a lot from the various expertise field of the particpants from geotechnical earthquake engineering to engineering seismology.

7 Acknowledgements

Such an exercise was made possible by the interest and funding of the French and Italian nuclear industry under the project "SIGMA". It was made successful thanks to the dedicated and proactive participation of many teams from all over the world: A large number of teams reacted very positively to our invitation to take part in this (risky) benchmarking exercise, among them the developers of a wide variety of internationally used constitutive laws and/or codes. Such a broad participation witnesses the actual need for such a carefully controlled comparison, and also brought an invaluable enrichment to the project, which undoubtedly

benefitted greatly from the deep expertise of the participants. PRENOLIN is part of two larger projects: SINAPS@, funded by the ANR (the French National Research Agency), and SIGMA, funded by a consortium of nuclear operators (EDF, CEA, AREVA, ENL).

8 References

Aki, K., Richards, P.G., 2002. Quantitative seismology.

Aubry, D., Hujeux, J.C., Lassoudiere, F., Meimon, Y., 1982. A double memory model with multiple mechanisms for cyclic soil behaviour, in: Proceedings of the Int. Symp. Num. Mod. Geomech. pp. 3–13.

Aubry, D., Modaressi, A., 1996. GEFDYN, Manuel scientifique. Éc. Cent. Paris LMSS-Mat.

Ausilio, E., Conte, E., Dente, G., Santini, A., Moraci, N., 2008. Seismic response of alluvial valleys to SH waves, in: AIP Conference Proceedings. p. 199.

Avila, M.P.S. d', Lenti, L., Semblat, J.-F., 2012. Modelling strong seismic ground motion: three-dimensional loading path versus wavefield polarization. Geophys. J. Int. 190, 1607–1624.

Bardet, J.P., Ichii, K., Lin, C.H., 2000. EERA: a computer program for equivalent-linear earthquake site response analyses of layered soil deposits. University of Southern California, Department of Civil Engineering.

Beresnev, I.A., Wen, K.-L., Yeh, Y.T., 1995. Nonlinear Soil Amplification: Its Corroboration in Taiwan. Bull. Seismol. Soc. Am. 85, 456–515.

Biot, M.A., 1956. Theory of Propagation of Elastic Waves in a Fluid-Saturated Porous Solid. I. Low-Frequency Range. J. Acoust. Soc. Am. 28, 168–178. doi:10.1121/1.1908239

Blanch, J.O., Robertsson, J.O., Symes, W.W., 1995. Modeling of a constant Q: Methodology and algorithm for an efficient and optimally inexpensive viscoelastic technique. Geophysics 60, 176–184.

Bonilla, L.F., Archuleta, R.J., Lavallée, D., 2005. Hysteretic and Dilatant Behavior of Cohesionless Soils and Their Effects on Nonlinear Site Response: Field Data Observations and Modeling. Bull. Seismol. Soc. Am. 95, 2373–2395.

Boore, D.M., Bommer, J.J., 2005. Processing of strong-motion accelerograms: needs, options and consequences. Soil Dyn. Earthq. Eng. 25, 93–115.

Brinkgreve, R.B.J., BROERE, W., WATERMAN, D., 2007. Plaxis 2D manual. Version.

Cundall, P., 2006. A simple hysteretic damping formulation for dynamic continuum simulations, in: Proceedings of the 4th International FLAC Symposium on Numerical Modeling in Geomechanics. Minneapolis: Itasca Consulting Group.

Dafalias, Y.F., Manzari, M.T., 2004. Simple plasticity sand model accounting for fabric change effects. J. Eng. Mech. 130, 622–634.

Darendeli, M.B., 2001. Development of a new family of normalized modulus reduction and material damping curves.

Day, S.M., Bradley, C.R., 2001. Memory-efficient simulation of anelastic wave propagation. Bull. Seismol. Soc. Am. 91, 520–531.

Day, S.M., Minster, J.B., 1984. Numerical simulation of attenuated wavefields using a Padé approximant method. Geophys. J. Int. 78, 105–118.

Derras, B., Bard, P.-Y., Cotton, F., Bekkouche, A., 2012. Adapting the Neural Network Approach to PGA Prediction: An Example Based on the KiK-net Data. Bull. Seismol. Soc. Am. 102, 1446–1461.

Elgamal, A., Yang, Z., Parra, E., Ragheb, A., 2003. Modeling of cyclic mobility in saturated cohesionless soils. Int. J. Plast. 19, 883 – 905. doi:http://dx.doi.org/10.1016/S0749-6419(02)00010-4

Foerster, E., Gélis, C., De Martin, F., Bonilla, L.-F., 2015. Numerical study of 1D/2D wave propagation in the Mygnodian basin, EUROSEISTEST, Northern Greece. 9ème Colloq. AFPS.

Gerolymos, N., Gazetas, G., 2006. Winkler model for lateral response of rigid caisson

foundations in linear soil. Soil Dyn. Earthq. Eng. 26, 347–361.
Gerolymos, N., Gazetas, G., 2005. Constitutive model for 1-D cyclic soil behaviour applied to seismic analysis of layered deposits. Soils Found. 45, 147–159.
Grammatikopoulou, A., Zdravkovic, L., Potts, D.M., 2006. General formulation of two kinematic hardening constitutive models with a smooth elastoplastic transition. Int. J. Geomech. 6, 291–302.
Graves, R.W., Day, S.M., 2003. Stability and accuracy analysis of coarse-grain viscoelastic simulations. Bull. Seismol. Soc. Am. 93, 283–300.
Hashash, Y.M.A., Groholski, D.R., Phillips, C.A., Park, D., Musgrove, M., 2012. DEEPSOIL 5.1. User Man. Tutor. 107.
Haskell, N.H., 1953. The dispersion of surface waves in multilayered media. Bull. Seismol. Soc. Am. 43, 17–34.
IAI, S., MATSUNAGA, Y., KAMEOKA, T., 1992. Strain space plasticity model for cyclic mobility. SOILS Found. 32, 1–15. doi:10.3208/sandf1972.32.2_1
Iai, S., Morita, T., Kameoka, T., Matsungaya, Y., Abiko, K., 1995. Response of a dense sand deposit during 1993 Kushiro-Oki earthquake. Soils Found. 35, 115–131.
Iai, S., Ozutsumi, O., 2005. Yield and cyclic behaviour of a strain space multiple mechanism model for granular materials. Int. J. Numer. Anal. Methods Geomech. 29, 417–442. doi:10.1002/nag.420
Iai, S., Tobita, T., Ozutsumi, O., Ueda, K., 2011. Dilatancy of granular materials in a strain space multiple mechanism model. Int. J. Numer. Anal. Methods Geomech. 35, 360–392. doi:10.1002/nag.899
Ishibashi, I., Zhang, X., 1993. Unified Dynamic shear moduli and damping ratio of sand and clay. Soils Found. 33, 182–191.
Ishihara, K., 1996. Soil Behaviour in Earthquake Geotechnics. Clarenton Press, Oxford.
ITASCA, F., 2011. 7.0: User Manual. Licence Number 213-039-0127-18973. Sapienza—Univ Rome Earth Sci. Dep.
Iwan, W.D., 1967. On a class of models for the yielding behavior of continuous and composite systems. J. Appl. Mech. 34, 612–617.
Johnston, D.H., Toksoz, M.N., Timur, A., 1979. Attenuation of seismic waves in dry and saturated rocks; II, Mechanisms. Geophysics 44, 691–711. doi:10.1190/1.1440970
Kontoe, S., 2006. Development of time integration schemes and advanced boundary conditions for dynamic geotechnical analysis. Imperial College London (University of London).
Kwok, A.O., Stewart, J.P., Hashash, Y.M., 2008. Nonlinear ground-response analysis of Turkey Flat shallow stiff-soil site to strong ground motion. Bull. Seismol. Soc. Am. 98, 331–343.
Leurer, K.C., 1997. Attenuation in fine-grained marine sediments; extension of the Biot-Stoll model by the “effective grain model” (EGM). Geophysics 62, 1465–1479. doi:10.1190/1.1444250
Liu, P., Archuleta, R.J., 2006. Efficient Modeling of Q for 3D Numerical Simulation of Wave Propagation. Bull. Seismol. Soc. Am. 96, 1352–1358. doi:10.1785/0120050173
Matasovic, N., Kavazanjian Jr, E., 2006. Seismic response of a composite landfill cover. J. Geotech. Geoenvironmental Eng. 132, 448–455.
Matasović, N., Ordóñez, G., 2007. D-MOD2000. GeoMotions, LLC, Computer Software.
Matasovic, N., vucetic, M., 1995. Generalized cyclic-degradation-pore-pressure generation model for clays. J. Geotech. Eng. 121, 33–43.
Matasovic, N., vucetic, M., 1993. Analysis of seismic records obtained on november 24, 1987 at the Wildlife liquefaction array. University of California, Los Angeles.
Moczo, P., Kristek, J., Gális, M., 2004. Simulation of the planar free surface with near-

surface lateral discontinuities in the finite-difference modeling of seismic motion. Bull. Seismol. Soc. Am. 94, 760–768.
Modaressi, H., Foerster, E., 2000. CyberQuake. User's Man. BRGM Fr.
Olsen, K., Day, S., Bradley, C., 2003. Estimation of Q for long-period (> 2 sec) waves in the Los Angeles basin. Bull. Seismol. Soc. Am. 93, 627–638.
Peyrusse, F., Glinsky, N., Gélis, C., Lanteri, S., 2014. A high-order discontinuous Galerkin method for viscoelastic wave propagation, in: Spectral and High Order Methods for Partial Differential Equations-ICOSAHOM 2012. Springer, pp. 361–371.
Phillips, C., Hashash, Y., 2009a. Damping formulation for nonlinear 1D site response analyses. Soil Dyn. Earthq. Eng. 29, 1143–1158.
Phillips, C., Hashash, Y.M.A., 2009b. Damping formulation for nonlinear 1D site response analyses. Soil Dyn. Earthq. Eng. 29, 1143 – 1158. doi:http://dx.doi.org/10.1016/j.soildyn.2009.01.004
Pisanò, F., Jeremić, B., 2014. Simulating stiffness degradation and damping in soils via a simple visco-elastic–plastic model. Soil Dyn. Earthq. Eng. 63, 98–109.
Puzrin, A.M., Shiran, A., 2000. Effects of the constitutive relationship on seismic response of soils. Part I. Constitutive modeling of cyclic behavior of soils. Soil Dyn. Earthq. Eng. 19, 305 – 318. doi:http://dx.doi.org/10.1016/S0267-7261(00)00027-0
Régnier, J., Cadet, H., Bonilla, L.., Bertand, E., Semblat, J.F., 2013. Assessing nonlinear behavior of soil in seismic site response: Statistical analysis on KiK-net strong motion data. Bull. Seismol. Soc. Am. 103, 1750–1770.
Rodriguez-Marek, A., Mantalva, G. 1, Cotton, F., Bonilla, F., 2011. Analysis of Single-Station Standard Deviation Using the KiK-net Data. Bull. Seismol. Soc. Am. 101, 1242–1258.
Sandıkkaya, M.A., Akkar, S., Bard, P.-Y., 2013. A Nonlinear Site-Amplification Model for the Next Pan-European Ground-Motion Prediction Equations. Bull. Seismol. Soc. Am. 103, 19–32.
Santisi d'Avila, M.P., Semblat, J.-F., Lenti, L., 2013. Strong Ground Motion in the 2011 Tohoku Earthquake: A One-Directional Three-Component Modeling. Bull. Seismol. Soc. Am. 103, 1394–1410.
Schanz, T., Vermeer, P.A., Bonnier, P.G., 1999. The hardening soil model: formulation and verification. 2000 Comput. Geotech. 281–296.
Schnabel, P.B., Lysmer, J., Seed, H.B., 1972. SHAKE : a computer program for earthquake response analysis of horizontally layered sites (report). Earthquake Engineering Research Centre, Berkeley, California.
Seed, H., 1969. 1. M. Idriss, Influence of soil conditions on ground motions during earthquakes, J. Soil Mech Found Div Amer Soc Civ Eng 95.
Semblat, J.F., 1997. Rheological Interpretation of Rayleigh Damping. J. Sound Vib. 206, 741–744. doi:10.1006/jsvi.1997.1067
Stewart, J., Kwok, A., 2009. Nonlinear Seismic Ground Response Analysis: Protocols and VerificaBon Against Array Data. PEER Annu. Meet. San Franc.-Present. 84.
Susumu Iai, T.K., Yoasuo Matsunaga, 1990. Strain space plasticity model for cyclic mobility (No. 4). port and harbour reasearch insitute.
Taborda, R., Bielak, J., 2011. Large-scale earthquake simulation: computational seismology and complex engineering systems. Comput. Sci. Eng. 13, 14–27.
Thomson, W.T., 1950. Transmission of elastic waves through a stratified solid. J. Appl. Phys. 21, 89–93.
Vucetic, M., Dobry, R., 1991. Effect of soil plasticity on cyclic response. J. Geotech. Eng. 117.
Yang, Z., Elgamal, A., Parra, E., 2003. Computational model for cyclic mobility and

associated shear deformation. J. Geotech. Geoenvironmental Eng. 129, 1119–1127.
Yu, G., Anderson, J.G., Siddharthan, R.A.J., 1993. On the characteristics of nonlinear soil response. Bull. Seismol. Soc. Am. 83, 218–244.
Zeghal, M., Elgamal, A.-W., Tang, H.T., Srepp, J.C., 1995. Lotung downhole array. II: Evaluation of soil nonlinear properties. J. Geotech. Eng. 121, 363–378.

9 List of Figures

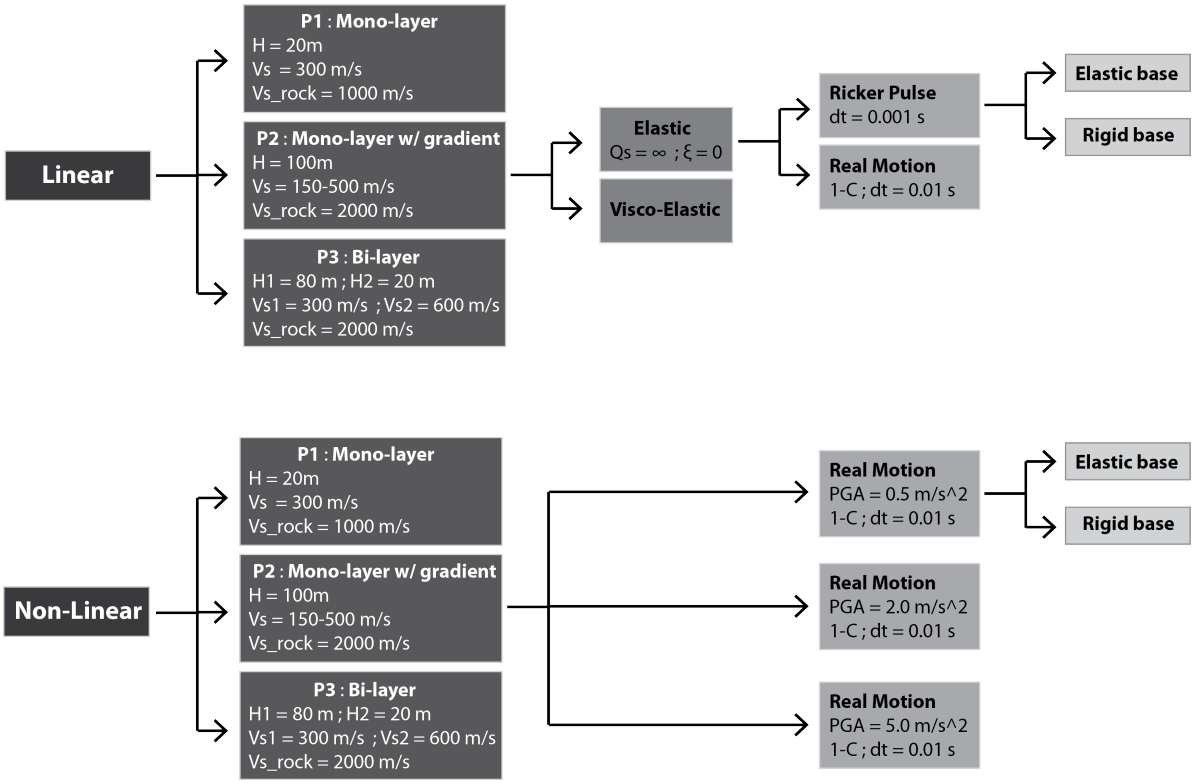
Linear
P1 : Mono-layer
H = 20m
Vs = 300 m/s
Vs_rock = 1000 m/s
P2 : Mono-layer w/ gradient
H = 100m
Vs = 150-500 m/s
Vs_rock = 2000 m/s
P3 : Bi-layer
H1 = 80 m ; H2 = 20 m
Vs1 = 300 m/s ; Vs2 = 600 m/s
Vs_rock = 2000 m/s
Elastic
Qs = ∞ ; ξ = 0
Visco-Elastic
Ricker Pulse
dt = 0.001 s
Real Motion
1-C ; dt = 0.01 s
Elastic base
Rigid base
Non-Linear
P1 : Mono-layer
H = 20m
Vs = 300 m/s
Vs_rock = 1000 m/s
P2 : Mono-layer w/ gradient
H = 100m
Vs = 150-500 m/s
Vs_rock = 2000 m/s
P3 : Bi-layer
H1 = 80 m ; H2 = 20 m
Vs1 = 300 m/s ; Vs2 = 600 m/s
Vs_rock = 2000 m/s
Real Motion
PGA = 0.5 m/s^2
1-C ; dt = 0.01 s
Real Motion
PGA = 2.0 m/s^2
1-C ; dt = 0.01 s
Real Motion
PGA = 5.0 m/s^2
1-C ; dt = 0.01 s
Elastic base
Rigid base

Figure 1

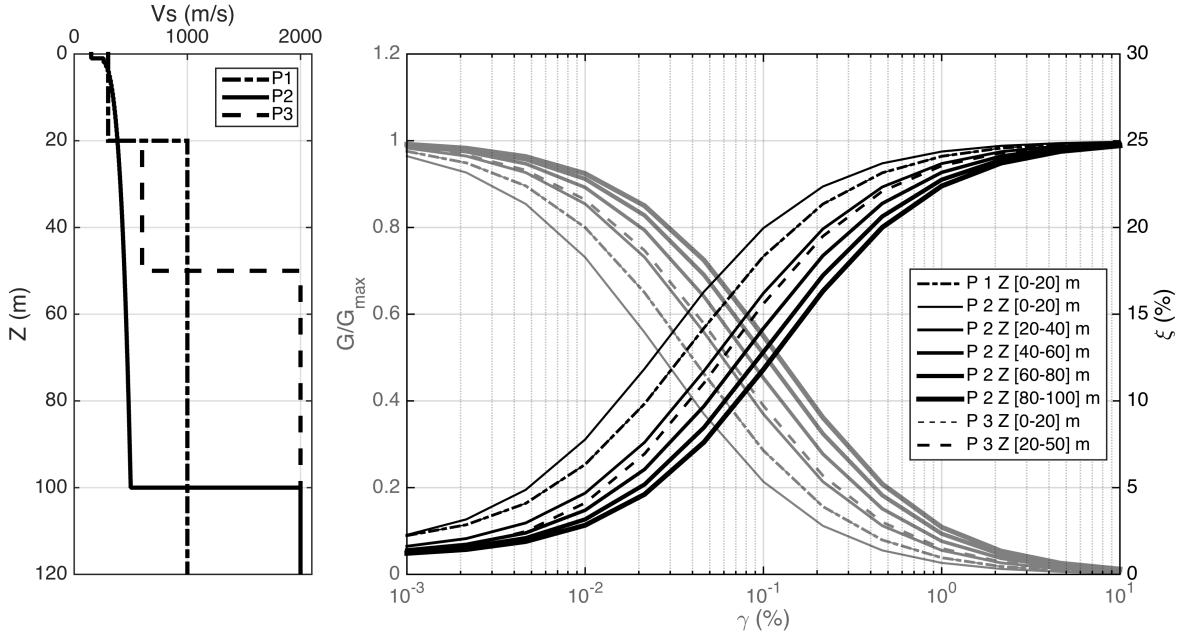
Vs (m/s)
0
1000
2000
Z (m)
P1
P2
P3
G/G_max
ξ (%)
γ (%)
P 1 Z [0-20] m
P 2 Z [0-20] m
P 2 Z [20-40] m
P 2 Z [40-60] m
P 2 Z [60-80] m
P 2 Z [80-100] m
P 3 Z [0-20] m
P 3 Z [20-50] m

Figure 2

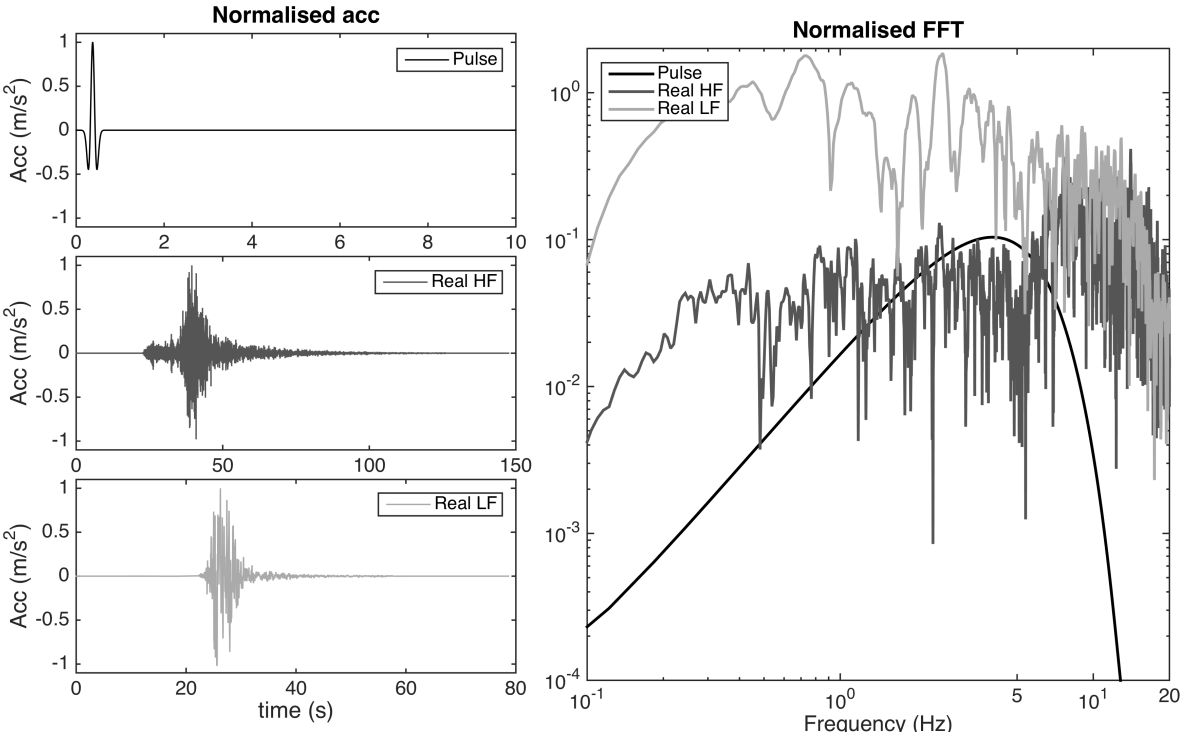
Normalised acc
Pulse
Real HF
Real LF
Acc (m/s^2)
time (s)
Normalised FFT
Pulse
Real HF
Real LF
Frequency (Hz)

Figure 3

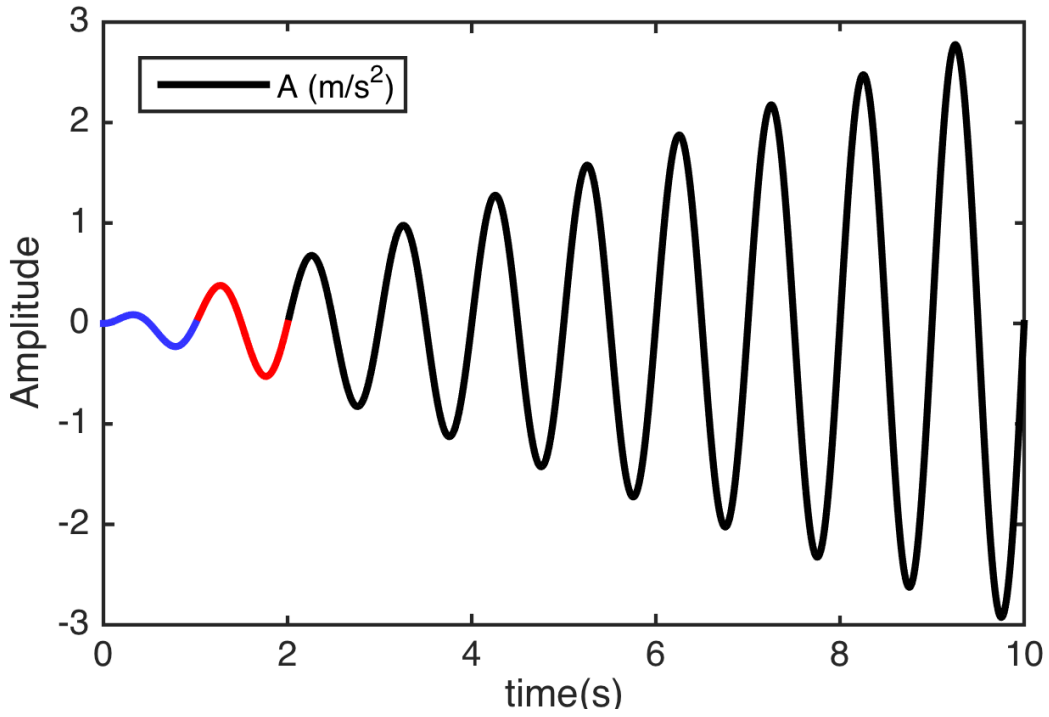

Figure 4

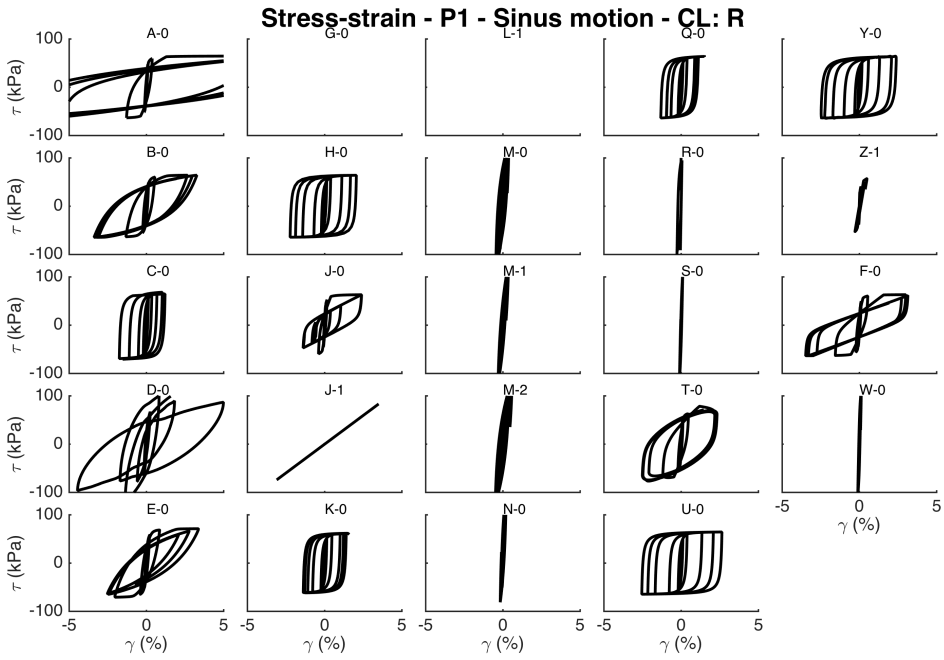
Stress-strain - P1 - Sinus motion - CL: R
A-0
G-0
L-1
Q-0
Y-0
B-0
H-0
M-0
R-0
Z-1
C-0
J-0
M-1
S-0
F-0
D-0
J-1
M-2
T-0
W-0
E-0
K-0
N-0
U-0
τ (kPa)
100
0
-100
-5
0
5
γ (%)

Figure 5

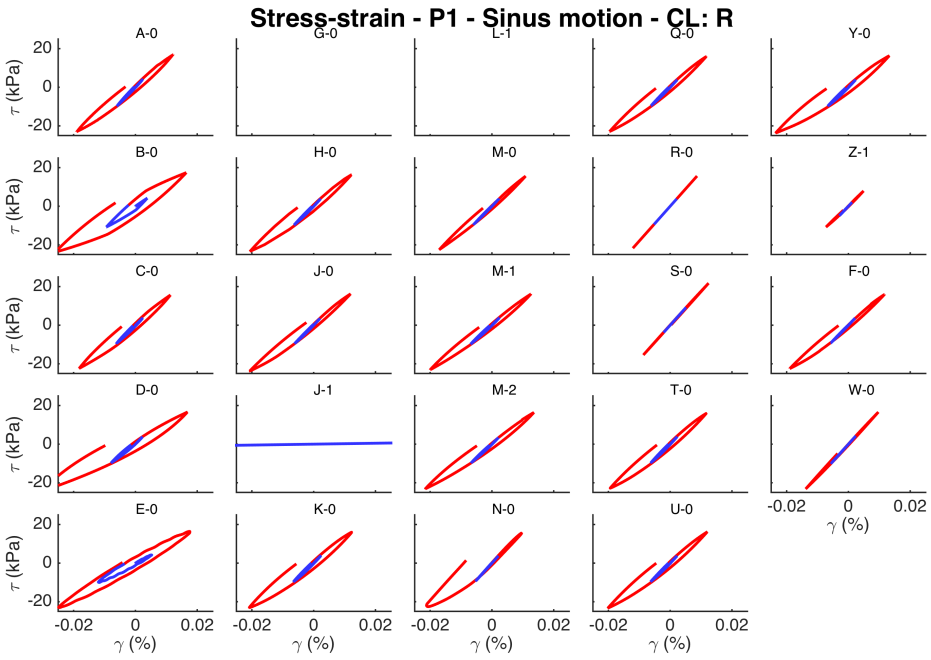
Stress-strain - P1 - Sinus motion - CL: R
A-0
G-0
L-1
Q-0
Y-0
B-0
H-0
M-0
R-0
Z-1
C-0
J-0
M-1
S-0
F-0
D-0
J-1
M-2
T-0
W-0
E-0
K-0
N-0
U-0
τ (kPa)
20
0
-20
-0.02
0
0.02
γ (%)

Figure 6

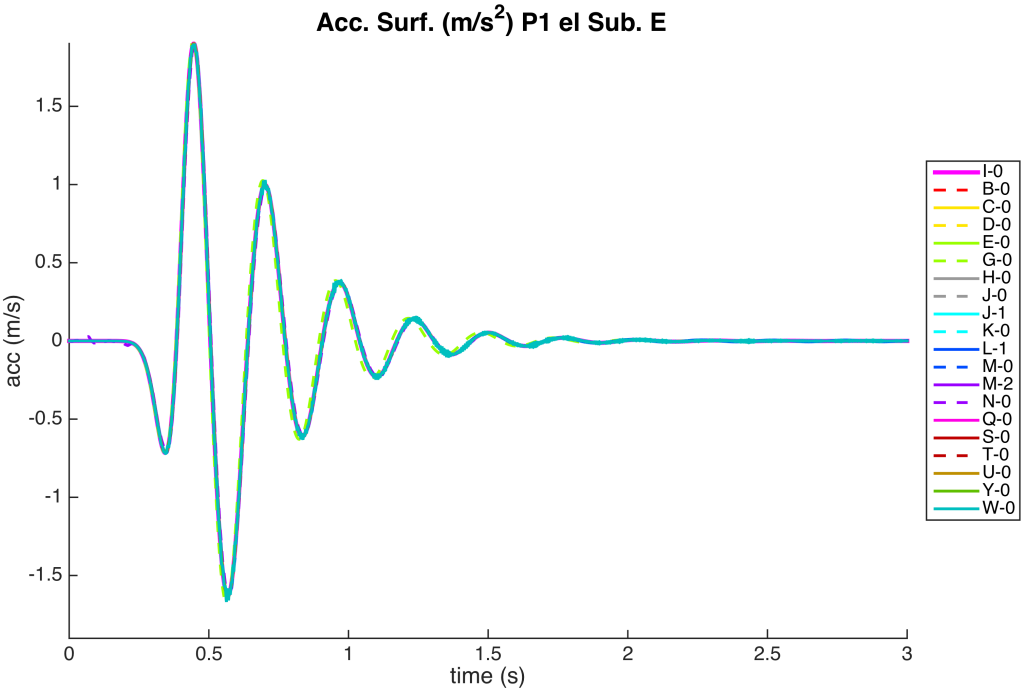
Acc. Surf. (m/s^2) P1 el Sub. E
acc (m/s)
time (s)
1.5
1
0.5
0
-0.5
-1
-1.5
0
0.5
1
1.5
2
2.5
3
I-0
B-0
C-0
D-0
E-0
G-0
H-0
J-0
J-1
K-0
L-1
M-0
M-2
N-0
Q-0
S-0
T-0
U-0
Y-0
W-0

Figure 7

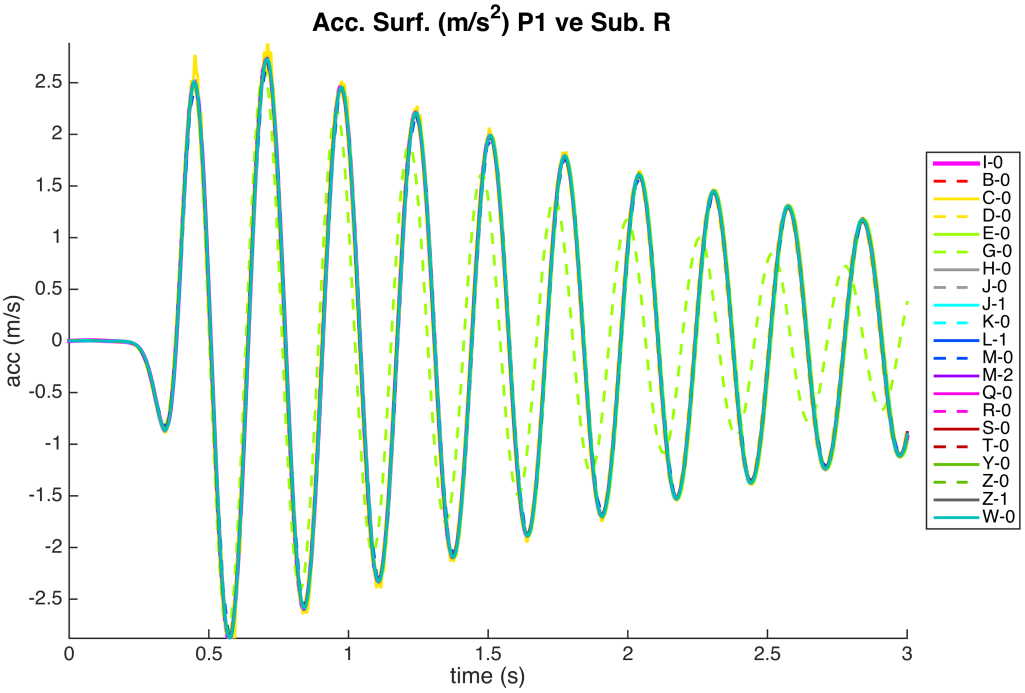
Acc. Surf. (m/s^2) P1 ve Sub. R
acc (m/s)
time (s)
2.5
2
1.5
1
0.5
0
-0.5
-1
-1.5
-2
-2.5
0
0.5
1
1.5
2
2.5
3
I-0
B-0
C-0
D-0
E-0
G-0
H-0
J-0
J-1
K-0
L-1
M-0
M-2
Q-0
R-0
S-0
T-0
Y-0
Z-0
Z-1
W-0

Figure 8

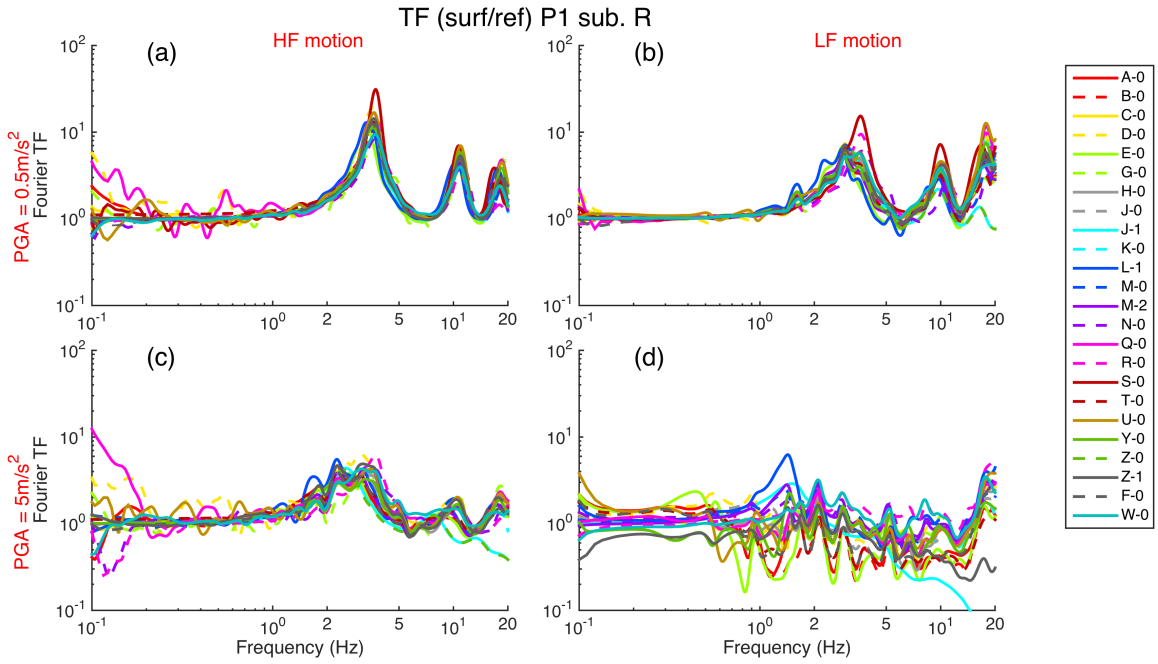
TF (surf/ref) P1 sub. R
HF motion
LF motion
(a)
(b)
(c)
(d)
PGA = 0.5m/s2
Fourier TF
PGA = 5m/s2
Fourier TF
Frequency (Hz)
Frequency (Hz)
A-0
B-0
C-0
D-0
E-0
G-0
H-0
J-0
J-1
K-0
L-1
M-0
M-2
N-0
Q-0
R-0
S-0
T-0
U-0
Y-0
Z-0
Z-1
F-0
W-0

Figure 9

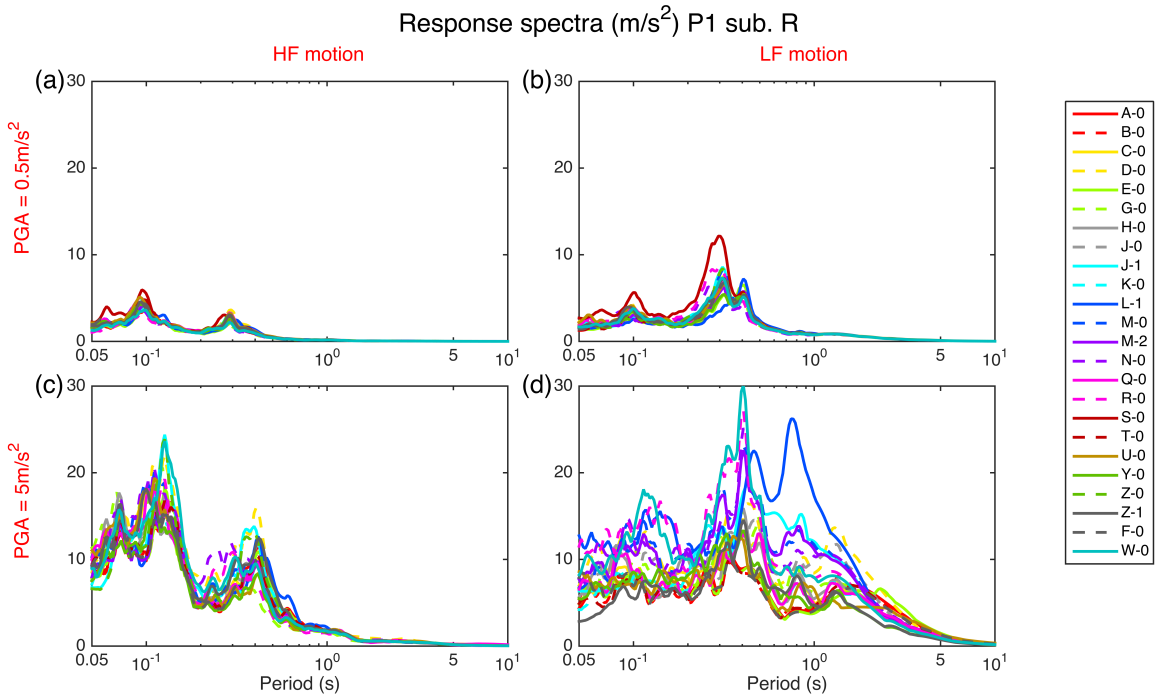
Response spectra (m/s^2) P1 sub. R
HF motion
LF motion
(a)
(b)
(c)
(d)
PGA = 0.5m/s^2
PGA = 5m/s^2
Period (s)
Period (s)
A-0
B-0
C-0
D-0
E-0
G-0
H-0
J-0
J-1
K-0
L-1
M-0
M-2
N-0
Q-0
R-0
S-0
T-0
U-0
Y-0
Z-0
Z-1
F-0
W-0

Figure 10

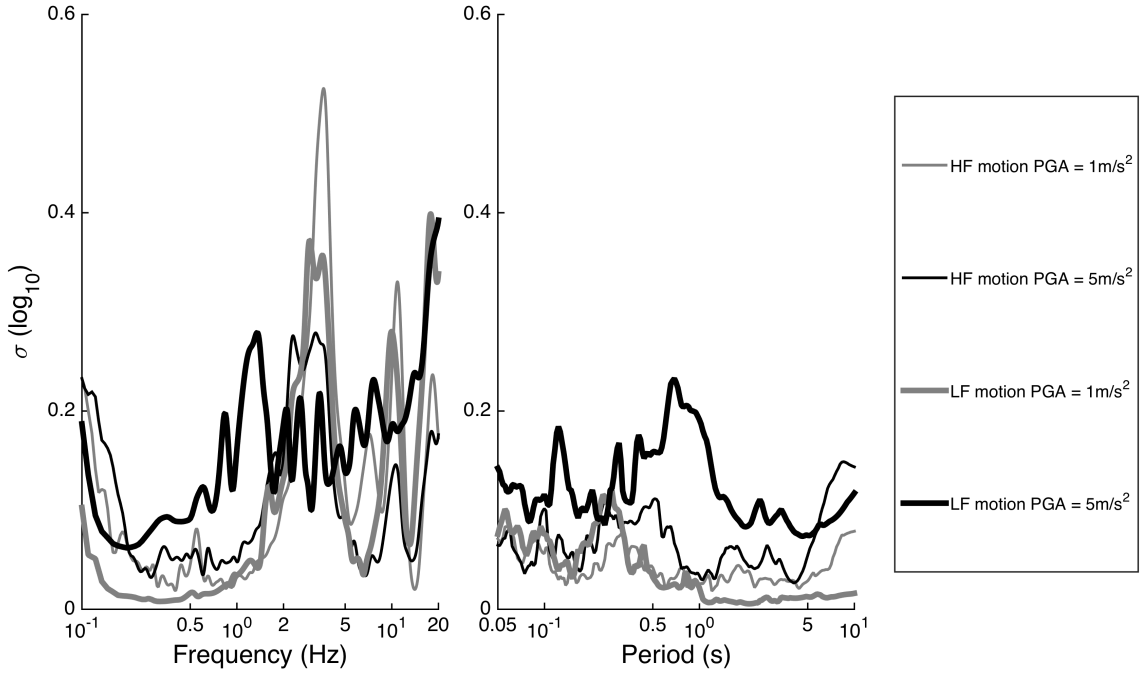
0.6
0.4
0.2
0
σ (log10)
10-1
0.5
100
2
5
101
20
Frequency (Hz)
0.05
Period (s)
HF motion PGA = 1m/s2
HF motion PGA = 5m/s2
LF motion PGA = 1m/s2
LF motion PGA = 5m/s2

Figure 11

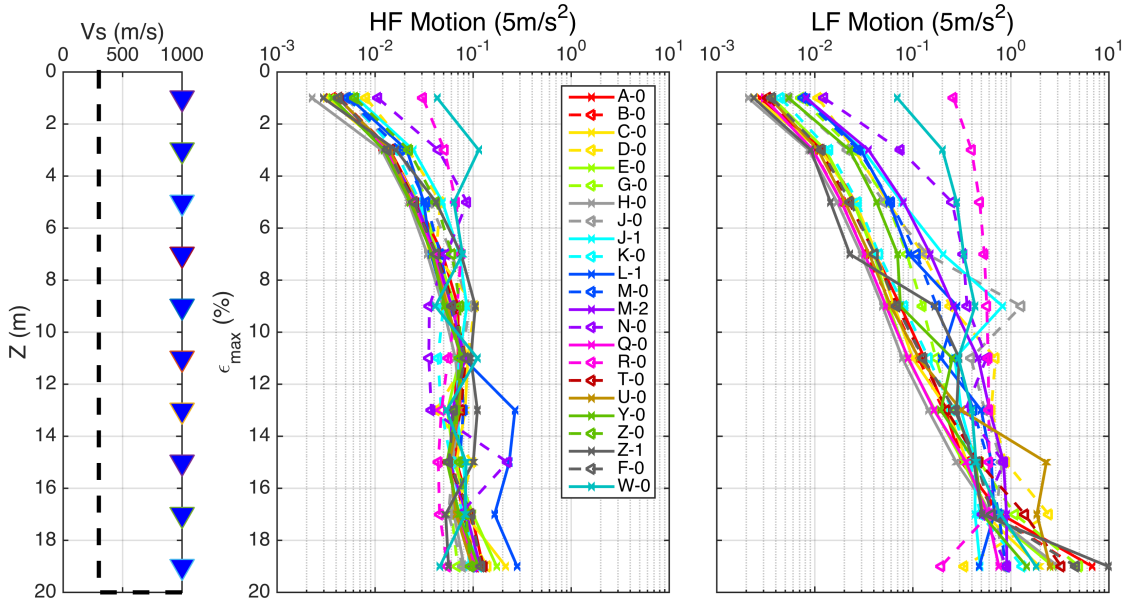
Vs (m/s)
0
500
1000
Z (m)
HF Motion (5m/s^2)
LF Motion (5m/s^2)
ϵ_{max} (%)
A-0
B-0
C-0
D-0
E-0
G-0
H-0
J-0
J-1
K-0
L-1
M-0
M-2
N-0
Q-0
R-0
T-0
U-0
Y-0
Z-0
Z-1
F-0
W-0

Figure 12

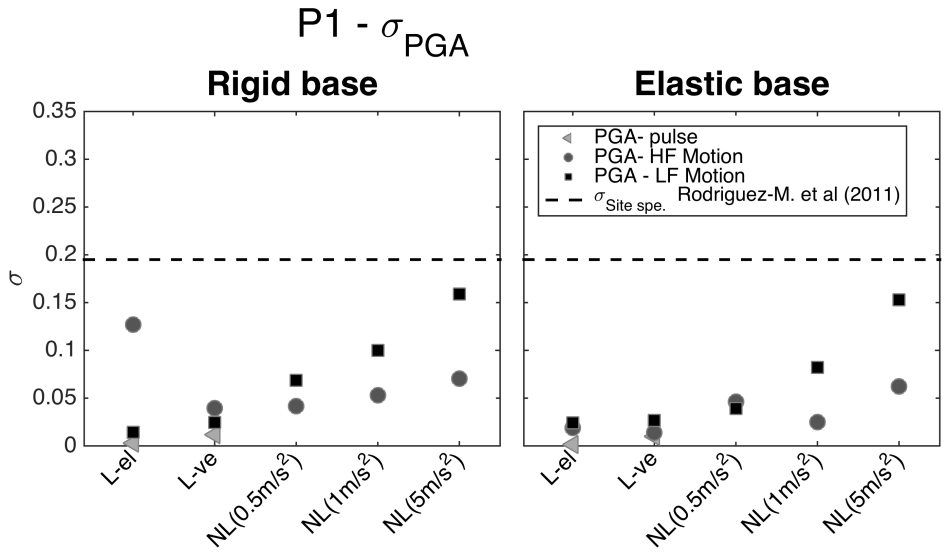
P1 - σ_{PGA}
Rigid base
Elastic base
PGA- pulse
PGA- HF Motion
PGA - LF Motion
$\sigma_{Site\ spe.}$ Rodriguez-M. et al (2011)
σ
0.35
0.3
0.25
0.2
0.15
0.1
0.05
0
L-el
L-ve
NL(0.5m/s^2)
NL(1m/s^2)
NL(5m/s^2)

Figure 13

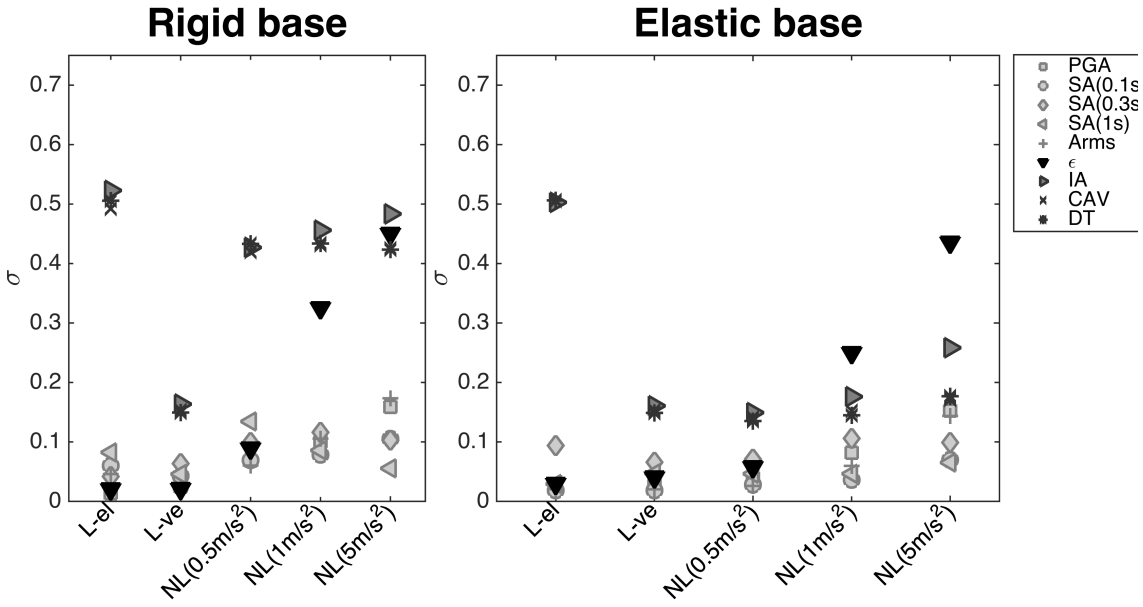
Rigid base
Elastic base
σ
0
0.1
0.2
0.3
0.4
0.5
0.6
0.7
L-el
L-ve
NL(0.5m/s²)
NL(1m/s²)
NL(5m/s²)
PGA
SA(0.1s
SA(0.3s
SA(1s)
Arms
ϵ
IA
CAV
DT

Figure 14

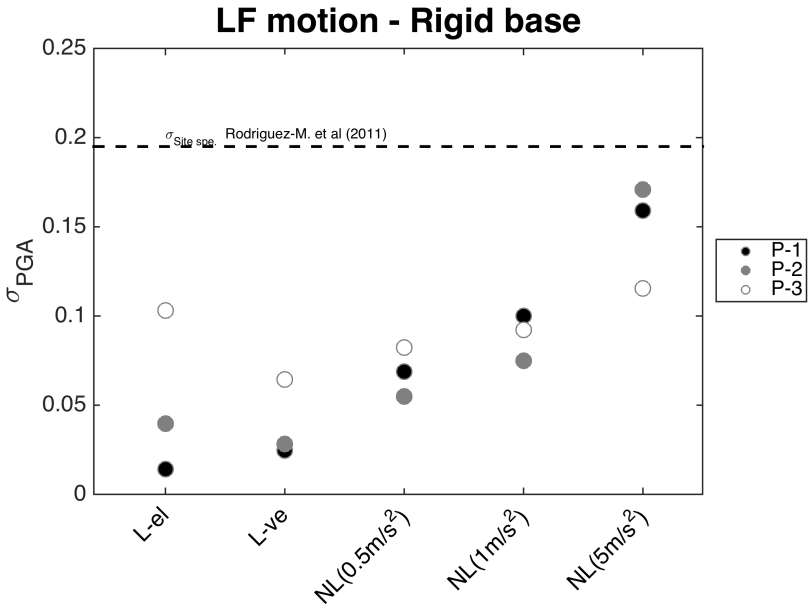
LF motion - Rigid base
0.25
0.2
0.15
0.1
0.05
0
σ_{PGA}
$\sigma_{Site\ spe.}$ Rodriguez-M. et al (2011)
P-1
P-2
P-3
L-el
L-ve
NL(0.5m/s^2)
NL(1m/s^2)
NL(5m/s^2)

Figure 15

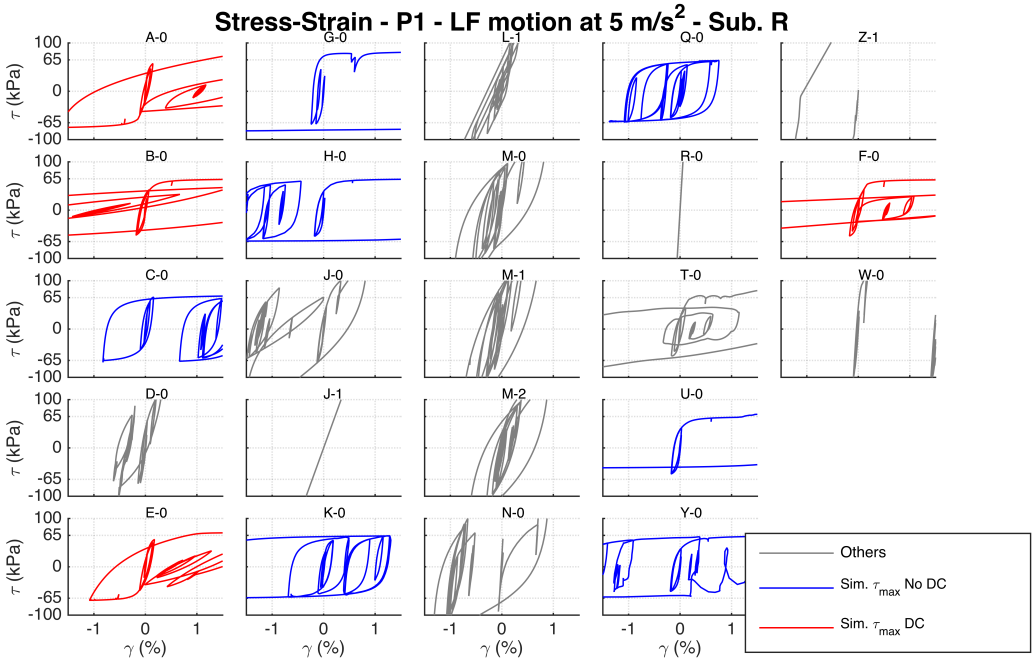
Stress-Strain - P1 - LF motion at 5 m/s^2 - Sub. R
A-0
G-0
L-1
Q-0
Z-1
B-0
H-0
M-0
R-0
F-0
C-0
J-0
M-1
T-0
W-0
D-0
J-1
M-2
U-0
E-0
K-0
N-0
Y-0
τ (kPa)
100
65
0
-65
-100
-1
0
1
γ (%)
Others
Sim. τ_{max} No DC
Sim. τ_{max} DC

Figure 16

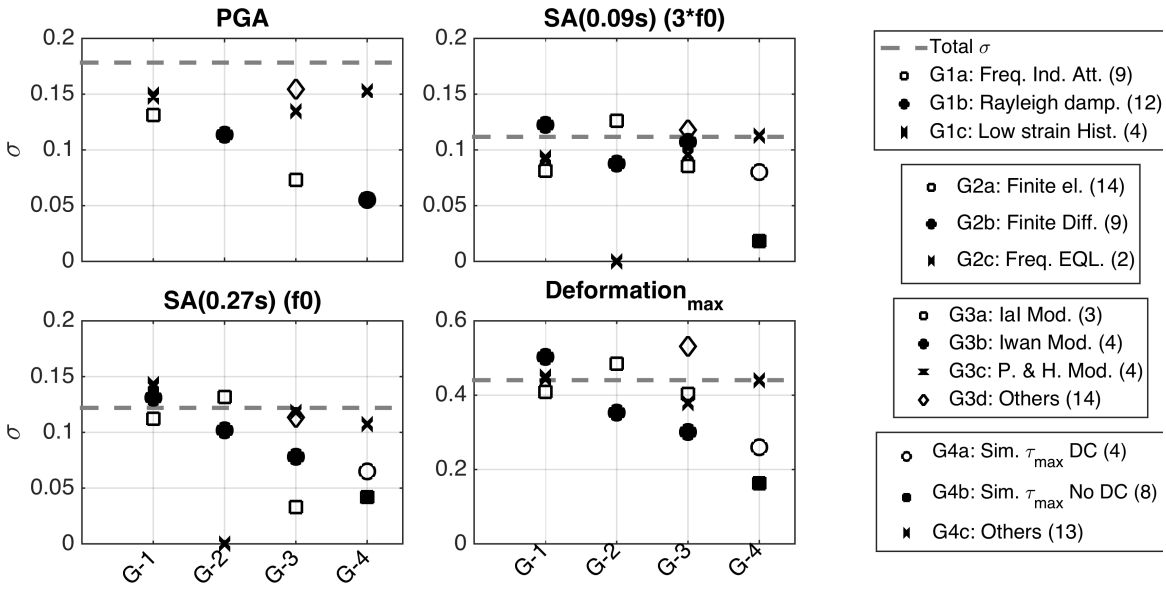
PGA
SA(0.09s) (3*f0)
SA(0.27s) (f0)
Deformation max
σ
0.2
0.15
0.1
0.05
0
0.6
0.4
G-1
G-2
G-3
G-4
Total σ
G1a: Freq. Ind. Att. (9)
G1b: Rayleigh damp. (12)
G1c: Low strain Hist. (4)
G2a: Finite el. (14)
G2b: Finite Diff. (9)
G2c: Freq. EQL. (2)
G3a: Ial Mod. (3)
G3b: Iwan Mod. (4)
G3c: P. & H. Mod. (4)
G3d: Others (14)
G4a: Sim. τmax DC (4)
G4b: Sim. τmax No DC (8)
G4c: Others (13)

Figure 17

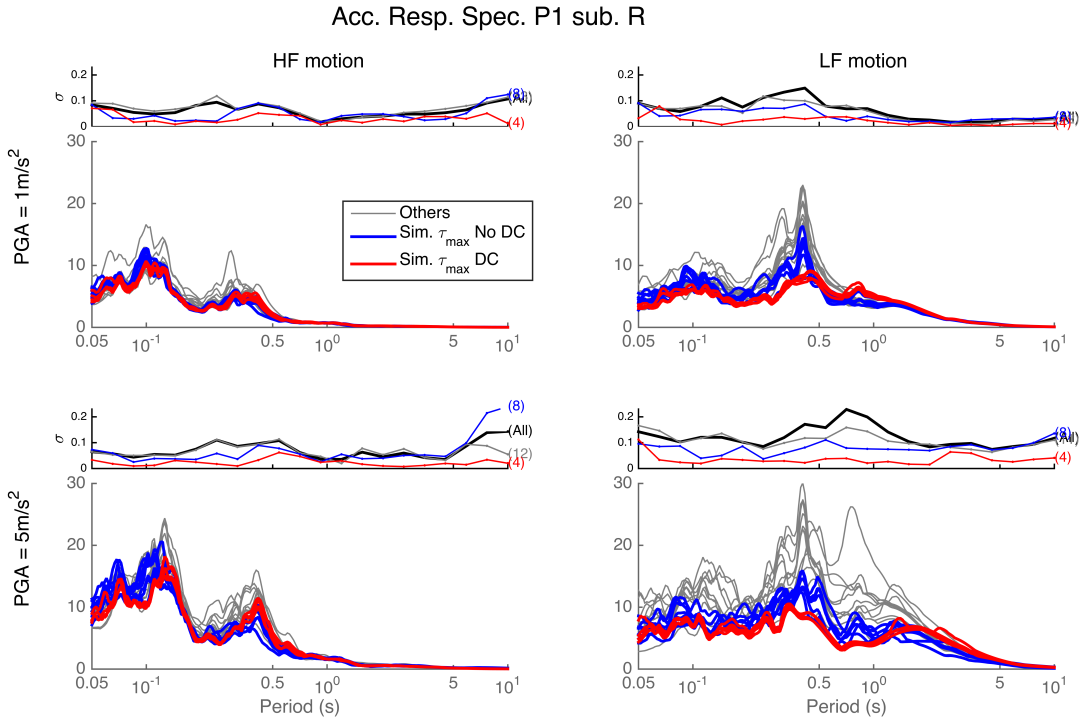
Acc. Resp. Spec. P1 sub. R
HF motion
LF motion
PGA = 1m/s2
PGA = 5m/s2
σ
Others
Sim. τmax No DC
Sim. τmax DC
(8)
(All)
(12)
(4)
Period (s)

Figure 18

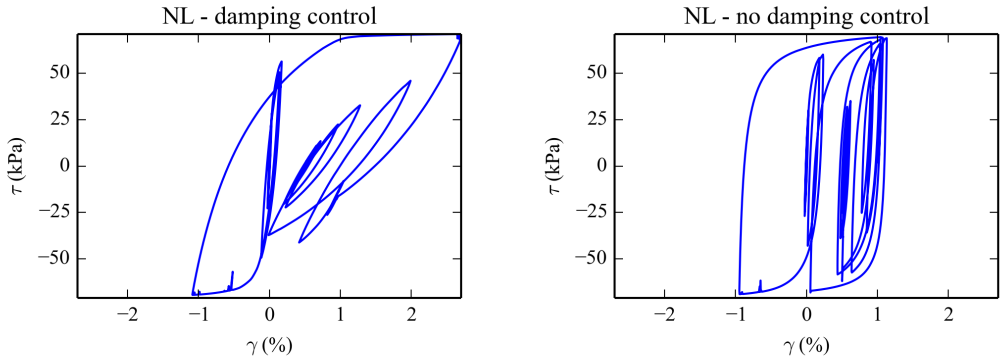
NL - damping control
NL - no damping control
τ (kPa)
γ (%)
50
25
0
−25
−50
−2
−1
0
1
2

Figure 19

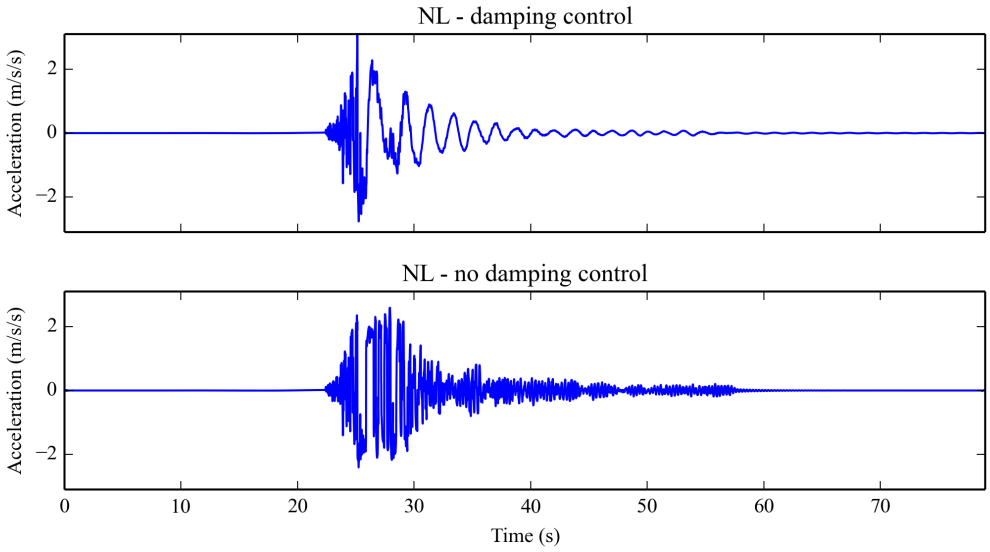
NL - damping control
Acceleration (m/s/s)
2
0
−2
NL - no damping control
Acceleration (m/s/s)
2
0
−2
0
10
20
30
40
50
60
70
Time (s)

Figure 20